nature communications

Article

https://doi.org/10.1038/s41467-026-69420-1

Granulomas microenvironment-guided sono-immunotherapy to treat and prevent recurrence of tuberculosis

Received: 28 July 2025

Accepted: 30 January 2026

Published online: 10 February 2026

Check for updates

Wei Wang[1,6], Fei Li[2,6], Wanying Mo[1,3,6], Zining Liu[1,6], Juan Xu[4], Yi Li[1,3], Peixian Weng[1,3], Zihui Liu[2], Pingqiang Cai[4], Shasha He[2] ✉, Yupeng Wang[1,3] ✉ & Dongfang Zhou[1,3,5] ✉

Curing tuberculosis (TB) remains challenging due to treatment complexity and high recurrence rates. Through bioinformatic analyses of the immune microenvironment within clinical non-tuberculous granulomas (NTBG)/tuberculous granulomas (TBG) samples, and peripheral blood from drug-resistant/sensitive, recurrent/non-recurrent TB patients, we identify suppression of innate immune responses, especially downregulated Toll-like receptor/NF-kappa B pathways in macrophages/dendritic cells and elevated B/T cell negative regulation, contributing to treatment failure and recurrence. Building on these insights, we develop mannose-modified organic semiconducting nano-immunostimulants (^{man}SNI) for precise TB sono-immunotherapy. Under optimized ultrasound condition, ^{man}SNI generates massive reactive oxygen species (ROS) to eradicate Mycobacterium tuberculosis (M.tb) within lung granulomas/macrophages, while simultaneously promoting in situ release of M.tb-derived antigens. The released antigens and TLR7 agonist R837 synergistically induce potent innate/adaptive anti-TB immunity and long-lasting immune memory. This granulomas microenvironment-guided sono-immunotherapy strategy demonstrates efficient TB control and relapse/reinfection prevention, which provides a promising direction for customized therapy against high-pathogenic infections.

Tuberculosis (TB), caused by *Mycobacterium tuberculosis* (M.tb), constitutes a persistent global health crisis with an estimated 1.7 billion latent infections worldwide[1]. This facultative intracellular pathogen demonstrates unique survival strategies through macrophage parasitism and granulomas formation—dynamic immune cell aggregates that paradoxically contain bacterial dissemination while establishing sanctuaries for antibiotic evasion and dormancy maintenance[2–4]. Current first-line multidrug regimens (6–24 months) frequently fail to completely eradicate M.tb infection[5], with alarming 2-year recurrence rates (6.7–18%)[6–8]. Consequently, challenging treatment regimens and

[1]NMPA Key Laboratory for Research and Evaluation of Drug Metabolism & Guangdong Provincial Key Laboratory of New Drug Screening & Guangdong-Hongkong-Macao Joint Laboratory for New Drug Screening, School of Pharmaceutical Sciences, Southern Medical University, Guangzhou, P. R. China. [2]College of Chemistry and Chemical Engineering, Innovation Laboratory for Sciences and Technologies of Energy Materials of Fujian Province (IKKEM), State Key Laboratory of Vaccines for Infectious Diseases, Xiang An Biomedicine Laboratory, Xiamen University, Xiamen, P. R. China. [3]Department of Pharmacy, The Seventh Affiliated Hospital, Southern Medical University, Foshan, P. R. China. [4]Jiangsu Key Laboratory of Molecular Medicine, Medical School, Nanjing University, Nanjing, P. R. China. [5]Key Laboratory of Mental Health of the Ministry of Education, State Key Laboratory of Multi-organ Injury Prevention and Treatment, Southern Medical University, Guangzhou, P. R. China. [6]These authors contributed equally: Wei Wang, Fei Li, Wanying Mo, Zining Liu. ✉e-mail: hss@xmu.edu.cn; wangyupeng5@i.smu.edu.cn; dfzhou@smu.edu.cn

a high incidence of TB recurrence present substantial obstacles in achieving an effective cure for this disease.

Currently, extensive research has been conducted on novel anti-TB small molecular drugs[9], adjuvant immunotherapy[10], and therapeutic vaccines[11], as well as emerging modalities such as photothermal therapy (PTT)[12] and photodynamic therapy (PDT)[13,14], which hold significant promise. However, these approaches still face limitations in completely eradicating M.tb and effectively addressing the issue of TB recurrence. Furthermore, the current focus of TB mechanism primarily revolves around the heterogeneity of granulomas and the correlation between specific cell types and bacterial load[15–17]. Nevertheless, there remains a lack of understanding regarding the characteristics of immune responses and the intricate interplay among different immune cell populations within granulomas, particularly in patients with drug-resistant and recurrent TB. These features may serve as critical factors contributing to treatment challenges and high recurrence rates[18]. Therefore, it is imperative to thoroughly investigate the immune response characteristics within tuberculous granulomas in order to guide the development of novel strategies for effectively controlling TB. Moreover, it is crucial to develop new treatment approaches based on these immune characteristics that can both eliminate M.tb and prevent TB recurrence.

In this work, to gain deeper insights into the mechanisms underlying drug resistance and TB recurrence, as well as to facilitate targeted treatment strategies, we conduct bioinformatic analyses of the immune microenvironment within clinical non-tuberculous granulomas (NTBG) samples, tuberculous granulomas (TBG) samples, and peripheral blood from drug-resistant *vs.* drug-sensitive and recurrent *vs.* non-recurrent TB patients at the single-cell RNA-sequencing (scRNA-seq) and transcriptomic analysis level. Our findings identify profound immunosuppression within TBG marked by downregulated Toll-like receptor (TLR) and NF-kappa B (NF-κB) signaling pathways in antigen-presenting cells (APCs), including macrophages and dendritic cells (DCs), alongside elevated negative immune regulation of B cell and T cell activities. The impaired intercellular crosstalk between these immune cells leads to severe immunosuppression within TBG, thus contributing to chemotherapy resistance and recurrence of TB. Based on the immunological microenvironment of TBG, we developed an organic semiconducting nano-immunostimulant (^{man}SNI) system equipped with a mannose warhead for highly precise TB sono-immunotherapy and recurrence prevention. Upon ultrasound irradiation, ^{man}SNI generates a large amount of ROS to precisely eliminate M.tb within lung granulomas and macrophages, while simultaneously promoting the in situ release of M.tb-derived antigens. The generated ROS can activate macrophages toward a pro-inflammatory state in combination with R837. Meanwhile, the release of M.tb-derived antigens and R837 from macrophages could synergistically promote DC maturation. These effects collectively trigger potent innate and adaptive anti-TB immune responses, including long-lasting immune memory. By remodeling the immunosuppressive microenvironment and augmenting the immune response, this sono-immunotherapy presents a promising avenue towards achieving a complete cure for TB while addressing the persistent issue of recurrence.

Results

Immune microenvironment characteristic analyses of TBG

Firstly, the heterogeneity of immune cells and cell-cell interactions was analyzed by collecting scRNA-seq datasets of 5 TBG samples, 12 NTBG samples, and 5 healthy lung samples from the Gene Expression Omnibus (GEO) public database[16]. Clinical information of these samples is summarized in Supplementary Table 1. A total of 11 immune cells and parenchymal cells were classified through cell-type-specific gene marker identification (Fig. 1a, and Supplementary Fig. 1a). Notably, TBG specimens exhibited marked alterations in cellular composition compared to both normal and NTBG subjects, particularly in immune cells populations such as macrophages, DCs, and T cells (Supplementary Fig. 1b). Among them, macrophages are the primary host cells of M.tb and key effector cells in anti-TB immunity, which can initiate the immune response through pathogen phagocytosis and cytokine secretion; DCs, as critical mediators bridging innate and adaptive immunity, facilitate antigen presentation to T cells to activate the adaptive immune response. However, TBG-associated macrophages[16] and DCs[19] demonstrated concurrent upregulation of immunosuppressive genes (ZFP36L2, TSC22D3, and DUSP1) and downregulation of immune activation-related genes (IL1B and CXCL8) compared to their counterparts in normal and NTBG subjects (Fig. 1b and c). Of particular significance, our analysis uncovered substantial impairment of canonical M.tb recognition and processing pathways, including NF-κB-, Nod-like receptor (NLR)-, and TLR signaling, as well as antigen processing mechanisms in TBG macrophages (Fig. 1d, e, Supplementary Fig. 2) and DCs (Fig. 1f, g, Supplementary Fig. 3). These findings collectively suggest compromised innate immune functionality characterized by defective antigen presentation in TBG, potentially contributing to delayed adaptive immunity activation. Consistent with this immunosuppressive characteristic, transcriptomic profiling of lymphocyte subsets revealed dual regulatory perturbations: upregulation of anti-inflammatory genes (such as IL10RB and DUSP1) and downregulation of pro-inflammatory genes (such as CCL20 and JUND) in $CD4^+$ T cells within the TBG (Supplementary Fig. 4). Furthermore, $CD4^+$ T cells and regulatory T cells (Tregs) exhibited enhanced activity of immune negative regulatory pathways (Fig. 1h and Supplementary Fig. 5). Similar functional inhibition was observed in natural killer (NK) cells in the TBG, with significant upregulation of "Negative regulation of lymphocyte activation" pathway and downregulation of "Natural killer cell mediated cytotoxicity and immunity" pathway (Fig. 1i, Supplementary Fig. 6). Notably, B cell functionality was also significantly attenuated in TBG specimens, as evidenced by suppressed activation markers and functional pathways (Fig. 1j, Supplementary Fig. 7). Cell Chat ligand-receptor interaction analysis further demonstrated disrupted intercellular communication between macrophages and other immune populations in TBG compared with the normal and NTBG groups (Fig. 1k and Supplementary Fig. 8), highlighting systemic immunosuppression through impaired immune cascades. Collectively, these findings confirm that the impairment of key M.tb recognition and antigen extraction pathways in macrophages and DCs within TBG leads to the suppression of the innate immune responses, and further weakens the overall immune function, providing a hotbed for the long-term survival and persistent infection of M.tb.

To investigate the clinical significance of immunosuppression in TBG, we further analyzed peripheral blood RNA-seq data from drug-resistant *vs.* drug-sensitive and recurrent vs. non-recurrent TB patients. The immune status of granulomas and peripheral blood is synchronized and correlated during TB infection[20]. Drug-resistant cases exhibited pronounced enrichment of immunosuppressive pathways compared with drug-sensitive cases (Fig. 1l), supported by a diagnostic model based on immune-negative regulatory differentially expressed genes (DEGs) with robust predictive accuracy across multiple machine learning algorithms (AUC 0.839; Fig. 1m; Supplementary Fig. 9). These findings strongly indicate that immunosuppression within TBG plays a critical role in influencing the drug resistance. The high recurrence rate is one of the major challenges in global TB prevention and control, and the low immunity of patients and the occurrence of drug resistance are important causes of incomplete anti-TB treatment and poor prognosis. Given the established correlation between granulomas, systemic immunity, and drug resistance, we hypothesize that TBG-mediated immunosuppression contributes to therapeutic failure and recurrence. Supporting this hypothesis, recurrent TB patients demonstrated relative upregulation of immunosuppressive genes (such as IDO1 and KIF14)[18] and relative down-regulation of immune activating genes (such as CD180[21], whose down-regulation can inhibit

https://doi.org/10.1038/s41467-026-69420-1

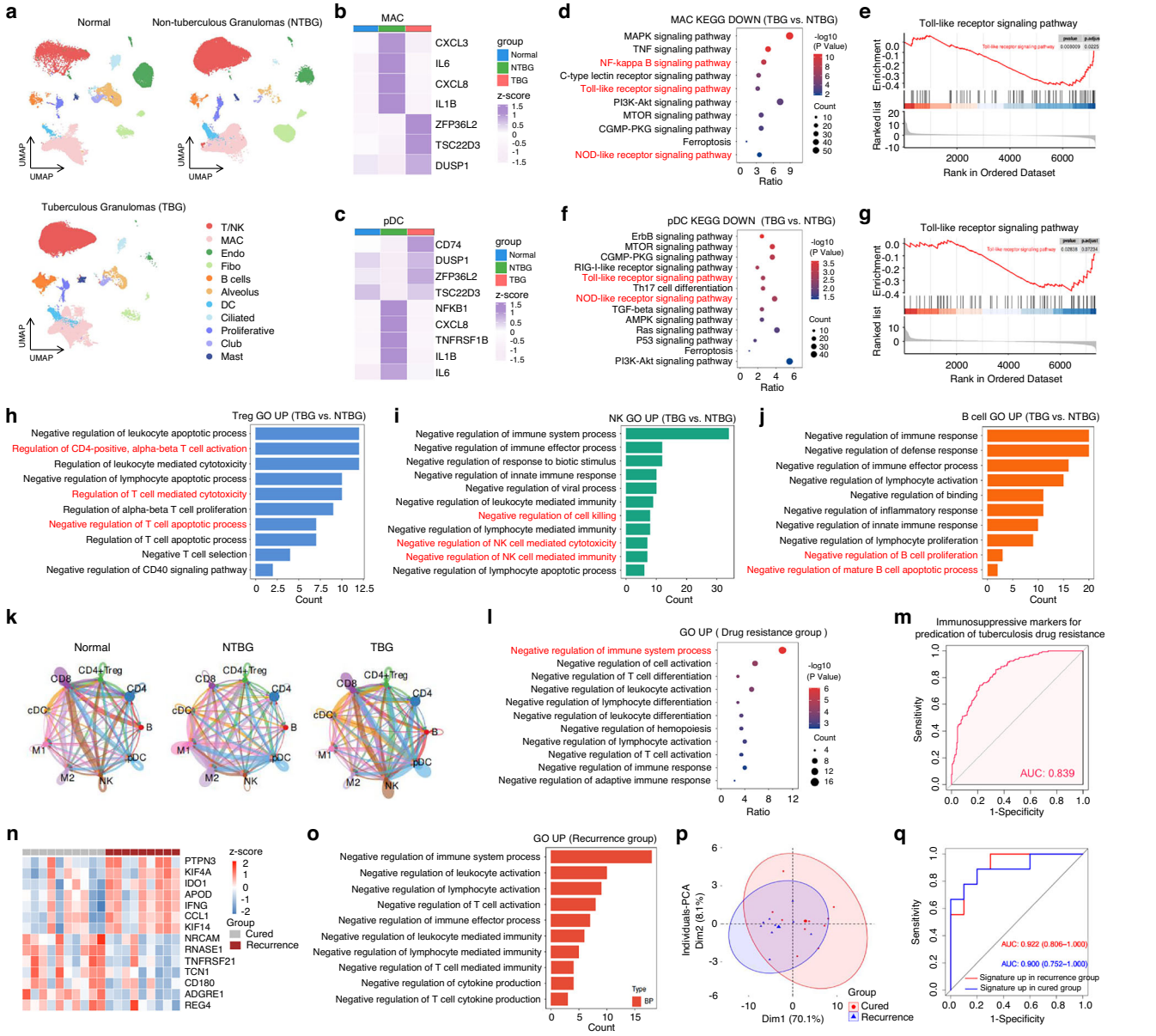

Fig. 1 | Immune microenvironment characteristic of TBG at the scRNA-seq and transcriptomic analysis level. a UMAP plot of cells from all scRNA-seq samples together, colored according to 11 cell types (normal, $n = 5$; NTBG, $n = 13$; TBG, $n = 5$, independent samples). Heatmap showing expression of DEGs of MAC (**b**) and pDC (**c**) (| log2FC| > 1, $p < 0.05$). The purple color denotes high expression, while the white color denotes low expression. KEGG enrichment analysis of the down-regulated DEGs in MAC (**d**) and pDC (**f**). (| log2FC| > 1, $p < 0.05$). Example gene set enrichment analysis (GSEA) of Toll-like receptor signaling pathway in MAC (**e**) and pDC (**g**). (| log2FC| > 1, $p < 0.05$). GO enrichment analysis of the upregulated DEGs in Treg cells (**h**), NK cells (**i**), and B cells (**j**). **k** Plots of the number and strength of interaction nets in the normal group, NTBG group, and TBG group. The greater the thickness of the line, the higher the number of contacts, and the more intense the interaction weights/strength between the two cell types. **l** KEGG enrichment analysis of the downregulated DEGs in drug resistance groups compare with the drug-sensitive groups. (|log2FC| > 1, $p < 0.05$). **m** The receiver operating characteristic curve (ROC) analysis. **n** Upregulated and downregulated DEGs involved in relapse (relapse group, $n = 9$; cured group, $n = 10$, independent samples) (|log2FC| > 1, $p < 0.05$). **o** GO enrichment analysis of the upregulated DEGs. **p** PCA was conducted on samples from the 9 patients with recurrence and the 10 cured patients using the 18 genes from the negative regulation of the immune system process pathway that were highly significantly expressed. **q** ROC analysis of 18 upregulated DEGs and 7 downregulated DEGs from the negative regulation of the immune system process pathway, and downregulated DEGs showed in **n** in the recurrent group. (The AUC was used as the metric to determine the effectiveness of the molecular signatures. log2FC, log 2-fold change. DEGs, differentially expressed genes. MAC macrophages, M1 classical activated macrophages, M2 alternatively activated macrophages, DCs dendritic cells, pDCs plasmacytoid dendritic cells, cDCs classical dendritic cells, GO gene ontology, PCA principal component analysis, ROC receiver-operating characteristic curve, AUC area under the curve, BP biological process, UMAP uniform manifold approximation and projection). For **d**–**g** and **l** statistical significance was calculated via one-way ANOVA with Tukey's post hoc test.

complement receptor type 3-mediated bacterial phagocytosis) compared with non-recurrent patients (Fig. 1n). Gene ontology (GO) enrichment analysis showed that many pathways associated with immune negative regulation were upregulated in recurrent patients (Fig. 1o). Meanwhile, the "Negative regulation of immune system process pathway" exhibited significant enrichment in DEGs analyses (Supplementary Fig. 10), indicating more severe immunosuppression among those with recurrent TB. Distinct separation was observed between the two sample groups based on 18 highly significant UP DEGs in the NRI pathway, and similar results were obtained using immune-

https://doi.org/10.1038/s41467-026-69420-1

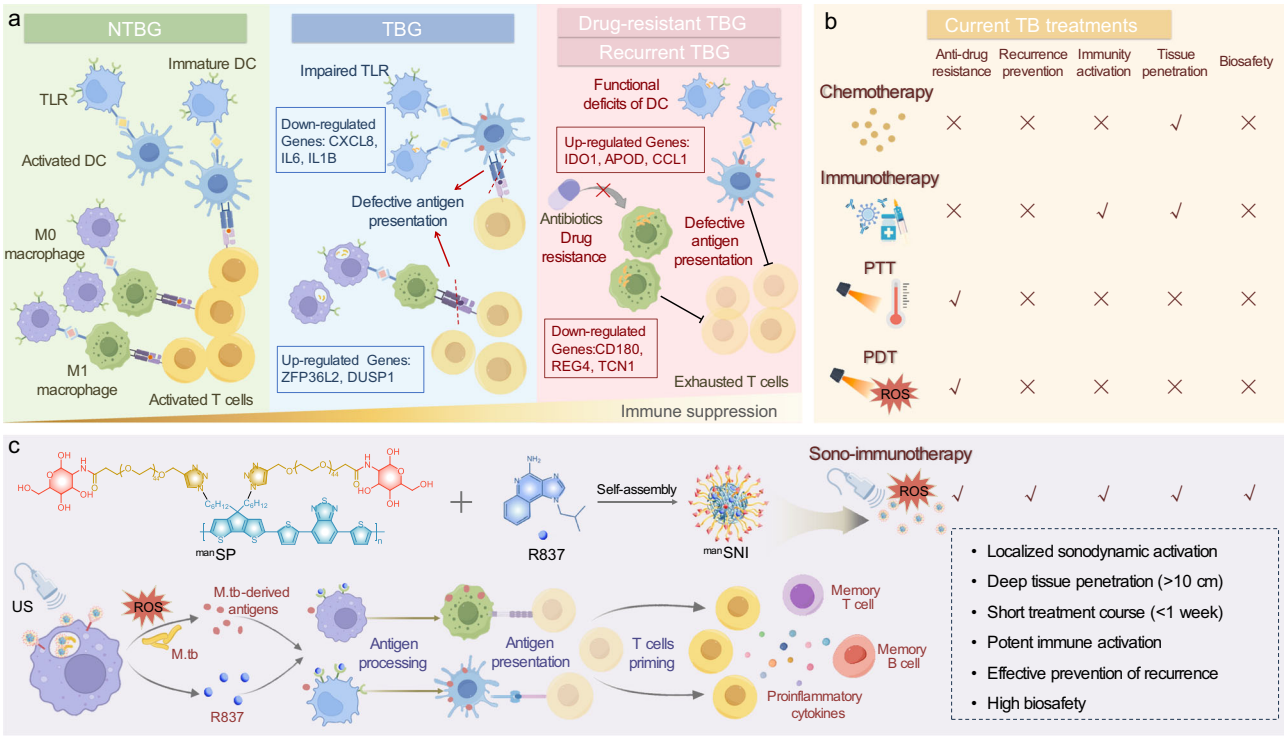

Fig. 2 | Concept design of granulomas immune microenvironment-guided TB sono-immunotherapy. a Schematic diagram of the immunosuppressive microenvironment of ordinary TBG, drug-resistant and recurrent TBG compared with NTBG. **b** Evaluation of current TB treatments, including chemotherapy, immunotherapy, PTT and PDT, based on anti-drug resistance, recurrence prevention, immunity activation, tissue penetration, and biosafety. **c** Schematic diagram of the structure of ^{man}SNI and action mechanism of ^{man}SNI-mediated TB sono-immunotherapy.

active DOWN DEGs (e.g., NRCAM, RNASE1)[22] (Fig. 1p and Supplementary Fig. 11). Diagnostic models incorporating these DEGs achieved near-perfect prediction of relapse outcomes (AUC 0.806-1.000; Fig. 1q; Supplementary Table 2). These multi-omics findings collectively establish TBG immunosuppression as a critical determinant of drug resistance development and post-treatment recurrence.

Collectively, our multi-omics analyses demonstrate that relative to NTBG, the immune microenvironment of TBG exhibits three hallmark suppressive features: (1) concomitant upregulation of immune checkpoint genes and functional impairment of pathogen recognition receptors (TLR/NLR/NF-κB pathways) in APCs including macrophages and DCs; (2) compromised cross-talk between innate and adaptive immunity, manifested by insufficient activation signals for cytotoxic lymphocytes (T/NK/B cells); and (3) progressive immunosuppression escalation in drug-resistant/recurrent TBG variants compared to ordinary TBG. This innate immunity impairment creates a self-perpetuating cycle-defective APC-mediated bacterial clearance synergizes with dysfunctional lymphocyte activation, collectively establishing delayed and suboptimal adaptive immune responses that permit M.tb persistence. Notably, the gradient of immunosuppressive severity (NTBG < ordinary TBG < drug-resistant/recurrent TBG) correlates directly with clinical refractoriness, suggesting microenvironmental immune paralysis as the linchpin of TB treatment failure (Fig. 2a). Taken together, our findings suggest the dual-action immune restoration-simultaneous potentiation of innate pathogen sensing and reinvigoration of cytotoxic lymphocyte functions—as a rational therapeutic strategy to overcome TBG-mediated immunosuppression, thereby breaking the vicious cycle of chronic infection and recurrence.

Preparation and in vitro anti-M.tb activity of ^{man}SNI

While conventional anti-TB regimens remain the cornerstone of clinical management, they face critical shortcomings in preventing disease recurrence. The protracted course of classic clinical standard chemotherapy (6–24 months) frequently results in compromised patient compliance, leading to treatment interruption, drug resistance, and relapse. Moreover, these nonspecific antibiotics induce substantial off-target toxicity, further exacerbating therapeutic challenges[23]. Current immunotherapeutic adjuncts (e.g., vaccine therapy, cytokine therapies, checkpoint inhibitors) attempt to potentiate antimicrobial immunity through host-directed strategies, which may reduce chemotherapy duration or mitigate adverse effects when combined with antimicrobials. However, their inability to replace antibiotics, heterogeneous patient responses, and risk of immune hyperactivation significantly limit clinical translation[24]. Emerging non-invasive modalities such as PTT and PDT offer mechanistically distinct advantages through an antibiotic-independent bactericidal mechanism and high spatial precision. Nevertheless, their limited tissue penetration depth (particularly problematic for pulmonary lesions) and phototoxic side effects restrict practical implementation (Fig. 2b)[25]. This therapeutic impasse underscores the urgent need for next-generation precision interventions capable of simultaneously achieving: (1) effective eradication of primary infection; (2) systemic immune potentiation; and (3) durable protection against recurrence. Sonodynamic therapy (SDT) is an emerging modality that employs ultrasound (US) to activate sonosensitizers for localized ROS generation[26]. Unlike optical modalities, US offers superior tissue penetration (>10 cm vs. < 3 cm for NIR light), enabling noninvasive treatment of deep-seated lesions[27]. Moreover, SDT ensures precise spatiotemporal control of treatment by adjusting the location, duration, and intensity of US irradiation without causing significant tissue damage. It has also been reported that SDT can induce immunogenic cell death, enhance antigen presentation, and promote immune activation[28,29]. As an extension of SDT, combining SDT-mediated pathogen killing with immune stimulation to elicit systemic anti-disease immunity is referred to as sono-immunotherapy. Hence, capitalizing on these mechanisms and based on our findings, we

engineered a organic semiconducting nano-immunostimulants (^{man}SNI) system for TB sono-immunotherapy featuring (Fig. 2c): (1) mannose-mediated active targeting of infected macrophages; (2) organic semiconducting polymers with highly elongated π-π conjugated backbones represent a class of sonodynamic inducer materials[30,31], exhibiting enhanced stability and efficiency in generating ROS compared to conventional counterparts[32,33]; and (3) TLR7 agonist Imiquimod (R837) payloads-an FDA-approved immunoadjuvant that synergistically activates type I interferon pathways APCs, thereby activating the innate and adaptive immunity[34]. Under US irradiation, ^{man}SNI are expected to orchestrate a tripartite therapeutic cascade: (i) focal ROS generation to clear localized M.tb and promote pathogen antigens release; (ii) release of antigens and R837 for synergistic driven APC activation to reverse immunosuppression of TBG; and (iii) pathogen-specific memory lymphocyte priming-collectively establishing a protective immune barrier against both endogenous relapse and exogenous reinfection.

Initially, an amphiphilic organic semiconducting polymer (SP) was synthesized as depicted in Fig. 3a. SPBr was obtained through palladium-catalyzed Stille polymerization by reacting monomer 1 (M1) and monomer 2 (M2) at a 1:1 ratio, followed by replacement of the bromine group with sodium azide to yield SPN_3. Subsequently, SPN_3 underwent click reaction with alkynyl-PEG-COOH to afford SP[35,36]. The amphiphilic SP can undergo self-assembly to form semiconducting nanoparticles (SN) with an average diameter of approximately 169 nm. Given that M.tb primarily colonizes granulomatous macrophages, D-mannosamine hydrochloride was modified on the PEG to obtain mannose-modified SP (^{man}SP)[37,38]. The structures of SP and ^{man}SP were characterized and confirmed using proton nuclear magnetic resonance spectroscopy (^{1}H NMR) (Supplementary Figs. 12–15). Subsequently, ^{man}SP could self-assemble into macrophage-targeted semiconducting nanoparticles (^{man}SN). Moreover, hydrophobic R837 was loaded into ^{man}SN during the self-assembly process to produce macrophage-targeted organic semiconducting nano-immunostimulants (^{man}SNI) (Fig. 3a). The resulting nanoparticles exhibited a spherical morphology and homogeneous size as observed in transmission electron microscopy (TEM) images (Fig. 3b and Supplementary Fig. 16). ^{man}SNI exhibited an average diameter of 178 nm and a negative surface zeta potential of −15.9 mV (Fig. 3c, d). After optimization, the final loading percentage of R837 in ^{man}SNI was determined to be around 2.3% using high-performance liquid chromatography (HPLC) (Supplementary Fig. 17).

The optical and physical properties of these semiconducting nanoparticles were then investigated. SN, ^{man}SN, and ^{man}SNI exhibited a similar maximum absorption peak at 630 nm (Fig. 3e) and characteristic emission peak at 827 nm (Fig. 3f), indicating that the modified side chain groups and loaded R837 had no impact on the optical properties of ^{man}SNI. Subsequently, the sonochemical activities of ^{man}SNI were evaluated by employing singlet oxygen sensor green (SOSG) to detect $^1O_2$ generation. Under ultrasound irradiation (1.5 W/cm^2, duty cycle of 50%, frequency of 1 MHz) for 5 min, ^{man}SNI demonstrated a significant enhancement in SOSG fluorescence intensity (F/F_0) at 520 nm with an increase of ~2.1-fold compared to PBS control (Fig. 3g). Furthermore, through electron paramagnetic resonance (EPR) spectra analysis using 5,5-Dimethyl-1-pyrroline N-oxide (DMPO) as a radical scavenger, it was observed that SN, ^{man}SN, and ^{man}SNI generated large amounts of hydroxyl radicals (•OH) with an EPR spectrum intensity ratio of approximately 1:2:2:1 (Fig. 3h, i and Supplementary Fig. 18), confirming their exceptional sonodynamic capabilities.

Encouraged by the superior ROS generation ability of ^{man}SNI under US irradiation, the anti-M.tb activity of ^{man}SNI was then investigated. Both the Bacillus Calmette-Guérin (BCG, which shares a high degree of genomic homology with M.tb and is an internationally recognized preliminary screening model for anti-TB drugs/therapies[39]) and the attenuated strain of M.tb H37Ra (ATCC25177) were used as the model bacteria. Firstly, the colony-forming units (CFU) assay revealed that these semiconducting nanoparticles (SN, ^{man}SN, and ^{man}SNI) were not toxic to BCG and H37Ra (Supplementary Fig. 19) in the absence of US irradiation. While even when isolated by a 5 cm thick pork tissue pad (Fig. 3j), the combination of these nanoparticles and US irradiation (1.5 W/cm^2, 1 MHz, 5 min) resulted in a bacterial death rate exceeding 99% (Fig. 3k, l). In contrast, due to the poor tissue penetration of light (1.5 W/cm^2, 808 nm, 5 min), the near-infrared photosensitizer represented by ICG cannot kill BCG when separated by a 5 cm-thick layer of pork tissue (Supplementary Fig. 20). Similarly, the live/dead bacterial viability assay demonstrated that ^{man}SNI exhibited excellent efficiency in killing BCG and H37Ra (Fig. 3m and Supplementary Fig. 21) under US irradiation. Then, the structural changes in BCG and H37Ra after different treatments were examined. As shown in scanning electron microscopy (SEM) images, the combination of these nanoparticles and US irradiation caused extensive damage to the body structure of BCG and H37Ra (Fig. 3n), resulting in an overall shriveled and concave shape of bacteria. The disruption of bacterial structure resulted in the leakage of cellular contents, as evidenced by protein leakage high to 0.22 μg/mL in solution from bacterial (10^7 CFU/mL) (Supplementary Fig. 22), which are expected to activate the body's immune response as pathogen antigens. These results demonstrate that ^{man}SNI can kill M.tb by generating a large amount of ROS through sonodynamic effect.

Sono-immunotherapy efficacy of ^{man}SNI against intracellular M.tb

M.tb primarily colonizes within the lysosomes of macrophages in TBG, highlighting the critical importance of targeted nanomedicine accumulation in infected macrophages and intracellular bacteria for effective eradication of intracellular M.tb[40]. To investigate the specific targeting ability of ^{man}SNI to macrophages, mouse monocyte-derived macrophages (Raw264.7 cells) were labeled with Lyso-tracker-green and co-cultured with SN or ^{man}SNI for 12 h, and observed by confocal laser scanning microscopy (CLSM). The red fluorescence emitted by ^{man}SNI was predominantly co-localized within the lysosomes following endocytosis, exhibiting significantly stronger signal intensity compared to SN (Fig. 4a). Approximately 2.5-fold higher uptake of ^{man}SNI by macrophages compared to SN was further confirmed by flow cytometry analysis (Fig. 4b). Subsequently, an intracellular bacterial model was established by treating Raw264.7 cells infected with green fluorescent protein-labeled BCG (GFP-BCG) with either SN or ^{man}SNI for 12 h (Fig. 4c). GFP-BCG was colocalized well with ^{man}SNI, as revealed by CLSM imaging, indicating the targeting capability of ^{man}SNI towards intracellular BCG (Fig. 4d).

The intracellular anti-M.tb efficacy was subsequently investigated. At a US time of 15 min and US intensity of 1.5 W/cm^2, ^{man}SNI (SN concentration: 100 μg/mL) killed over 99% of intracellular BCG (Supplementary Fig. 23) and H37Ra (Supplementary Fig. 24) with no significant decrease in the viability of Raw264.7 cells (Supplementary Fig. 27). In contrast, SN and ^{man}SN exhibited only ~49.3% and ~66.9% killing efficiency of intracellular BCG and ~49.3% and ~66.9% killing efficiency of intracellular H37Ra under the same irradiation conditions, respectively (Fig. 4e, f). Therefore, ^{man}SNI can efficiently and selectively kill intracellular M.tb but not macrophages under the optimized US conditions (Supplementary Fig. 25). To further verify sonodynamic-induced generation of intracellular ROS for M.tb killing, the ROS indicator dichlorodihydrofluorescein diacetate (DCFDA) was employed. After US irradiation, ^{man}SNI induced a significantly 1.48-fold and 3.69-fold higher level of intracellular ROS compared to ^{man}SN and SN, respectively (Fig. 4g, h). These results highlight the superior intracellular anti-M.tb efficacy achieved by ^{man}SNI compared to SN and ^{man}SN counterparts. Furthermore, it is worth noting that even at drug concentrations (based on SN) up to 320 μg/mL, both Raw264.7 cells and normal

https://doi.org/10.1038/s41467-026-69420-1

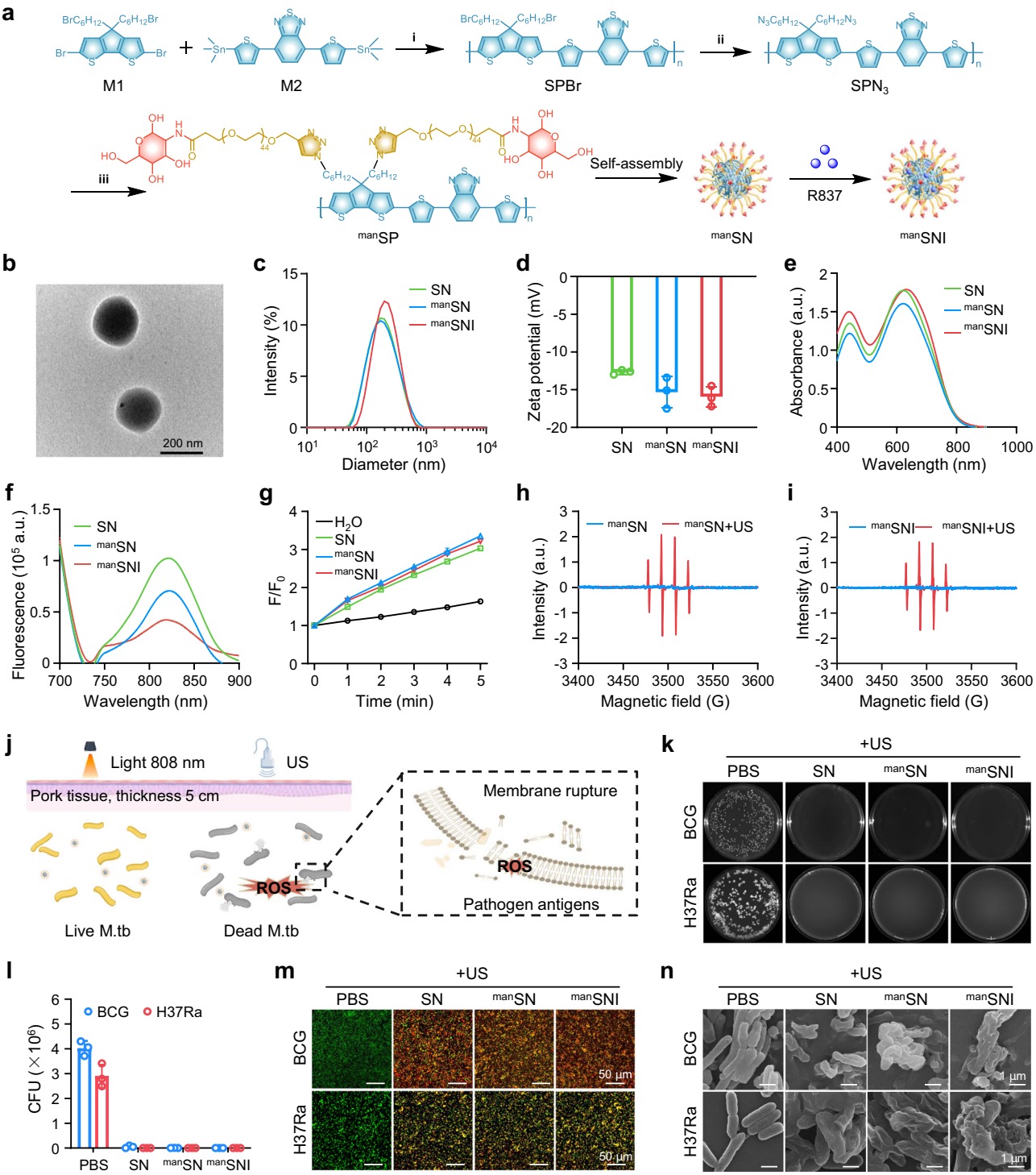

Fig. 3 | Preparation and in vitro anti-M.tb activity of ^{man}SNI. a A schematic illustration showing the preparation of ^{man}SNI (i. $PdCl_2(PPh_3)_2$, Tri-o-tolylphosphine, chlorobenzene, 100 °C, 30 min. ii. NaN_3, N,N-dimethylformamide (DMF), tetrahydrofuran (THF), 25 °C, 12 h. iii. CuBr, N,N,N′,N″,N‴-pentamethyldiethylenetriamine (PMDETA), alkynyl-PEG-COOH, THF, D-mannosamine hydrochloride). **b** TEM image of ^{man}SNI. **c** DLS of SN, ^{man}SN, and ^{man}SNI. **d** Surface Zeta potential of SN, ^{man}SN, and ^{man}SNI ($n = 3$ independent samples). **e** UV–vis absorption spectra of SN, ^{man}SN, and ^{man}SNI. **f** Fluorescence emission spectra of SN, ^{man}SN, and ^{man}SNI. **g** Detection of $^1O_2$ generation measured by SOSG probe ($n = 3$ independent samples). Electron paramagnetic resonance spectra for ^{man}SN (**h**) and (**i**) ^{man}SNI with or without US irradiation. **j** Schematic diagram of the anti-M.tb action mechanism of ICG-mediated PTT and ^{man}SNI-mediated SDT. 5 cm-thick pork tissue placed between the light/ultrasonic instrument and the test tube containing M.tb (1.5 W/cm^2, 1 MHz, 5 min). **k** Representative images showing the survival of BCG and H37Ra in the culture plate. **l** Quantitative statistics of the number of BCG colonies and H37Ra colonies through standard plate counting assay ($n = 3$ independent bacteria samples). **m** SYTO 9/PI staining assay of BCG and H37Ra after treatment with PBS, SN, ^{man}SN, and ^{man}SNI under US irradiation. **n** SEM images of BCG and H37Ra after being treated with PBS, SN, ^{man}SN, and ^{man}SNI under US irradiation. For **d**, **g** and **l** data are shown as the mean ± s.d., statistical significance was calculated via one-way ANOVA with Tukey's post hoc test. Experiments were repeated independently three times with similar results in **b**, **m** and **n** and a representative result is shown for each. (a.u. arbitrary units, F/F_0 fluorescence intensity/Initial fluorescence intensity).

https://doi.org/10.1038/s41467-026-69420-1

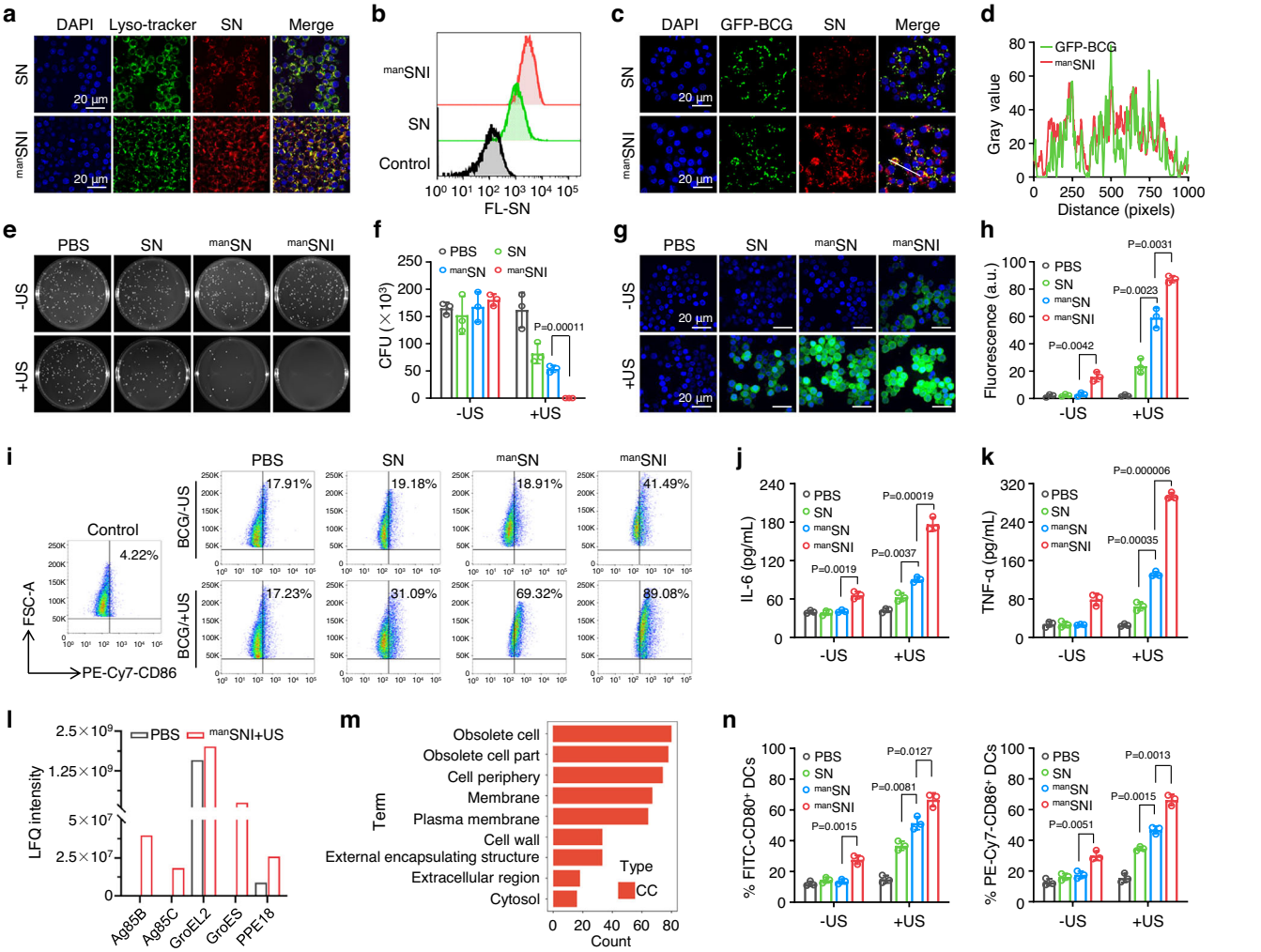

Fig. 4 | In vitro targeting and sono-immunotherapy efficacy of ^{man}SNI against intracellular M.tb. a CLSM images of activated Raw264.7 cells (Lyso-tracker) after incubation with SN, ^{man}SNI for 12 h. Scale bar: 20 μm. **b** The flow cytometry quantified assay of the endocytosis of SN and ^{man}SNI in Raw264.7 cells. **c** CLSM images of intracellular GFP-BCG after incubation with SN, ^{man}SNI for 24 h. Colocalization analysis was performed on the cells labeled by the white line. Scale bar: 20 μm. **d** Fluorescence intensity profiles across the merged images of GFP-BCG and ^{man}SNI. Representing photographs (**e**) and quantitative statistics (**f**) of the number of intracellular BCG formed on 7H10-agar plates after different treatments. The BCG-infected Raw264.7 cells were co-incubated with PBS, SN, ^{man}SN, or ^{man}SNI (based on SN concentration: 100 μg/mL) for 12 h and then either sonicated for 15 min (1.5 W/cm^2) or not sonicated. ($n = 3$ independent cell samples). Fluorescent images (**g**) and quantitative analysis (**h**) of ROS production in BCG-infected Raw264.7 cells after different treatments. Scale bar: 20 μm ($n = 3$ independent cell samples). **i** Representative flow cytometry plots of M1-type BCG-infected Raw264.7 cells (CD86$^+$) after different treatments. The no BCG-infected Raw264.7 cells served as the control group. j, k, IL-6 (**j**) and TNF-α (**k**) concentrations in the culture medium of BCG-infected Raw264.7 cells after PBS and manSNI treatments ($n = 3$ independent cell samples). **l** Amount of BCG-derived antigens (analyzed by Label-Free Quantification, LFQ) in supernatant of BCG-infected Raw264.7 cells after different treatments detected by mass spectrometry. **m** GO enrichment analysis of BCG-derived antigens after different treatments. **n** Quantification of mDCs (CD80$^+$ or CD86$^+$) after flow cytometry analysis. Data are represented as mean ± SD ($n = 3$ independent cell samples). For **f**, **h**, **j**, **k** and **n** data are shown as the mean ± s.d., statistical significance was calculated via one-way ANOVA with Tukey's post hoc test. Experiments were repeated independently three times with similar results in **a** and **c** and a representative result is shown for each (a.u., arbitrary units, LFQ label-free quantification).

mouse fibroblast L929 cells exhibited minimal toxicity when exposed to ^{man}SNI treatment without US (Supplementary Fig. 26), confirming its excellent biocompatibility.

Appropriate levels of ROS and R837 have been reported to enhance macrophage polarization towards a pro-inflammatory (M1) phenotype and increase the release of inflammatory cytokines by activating NF-κB signaling[41–43]. Flow cytometry showed that ^{man}SNI induced 2.1–2.3-fold higher population of M1 macrophages (CD86$^+$) compared to PBS, SN, and ^{man}SN in the absence of US irradiation (Fig. 4i). Moreover, in the presence of US irradiation, ^{man}SNI further increased the polarization of M1 macrophages by 5.2-fold compared to PBS group, and also induced 4.2-fold and 11.6-fold higher levels of pro-inflammatory cytokines IL-6 and TNF-α than that of PBS, respectively (Fig. 4j, k). These results indicate that ^{man}SNI + US irradiation treatment can largely activate macrophages to trigger the innate immune response. The above extracellular bacterial experiments showed the destruction of bacterial structure induced by ^{man}SNI + US irradiation, which resulted in the leakage of proteins (Supplementary Fig. 22). Here, the ^{man}SNI-mediated sonodynamic inducement of intracellular bacterial antigen presentation was further validated. The cell supernatant collected from BCG-infected macrophages after treatment was subjected to mass spectrometry analysis for identification. Compared to PBS, ^{man}SNI + US irradiation significantly enhanced the abundance of proteins and peptides in the cell supernatant, with a predominant association observed with cellular membrane and metabolic pathways (Supplementary Figs. 27–29). Importantly, abundant BCG-derived antigens, including Ag85 and PPE, were detected, which belong to a broad class of pro-inflammatory molecules known to enhance anti-TB

immune response (Fig. 4l)[44,45]. Furthermore, GO enrichment analysis revealed that the Cellular Component (CC) category encompassed various BCG cellular structures, particularly important pathways such as the cell periphery, cell wall, and membrane (Fig. 4m). These results demonstrate that ^{man}SNI + US irradiation can kill BCG and produce a large number of BCG-derived antigens, which are released outside macrophages through exocytosis[46]. These released BCG-derived antigens, along with adjuvant R837, can be transported to APCs, such as DCs, thereby promoting anti-TB adaptive immunity. Therefore, immature BMDCs and infected macrophages were co-cultured in a transwell plate (Supplementary Fig. 30). In the absence of US irradiation, ^{man}SNI treatment resulted in significantly upregulated levels of CD80 (2.81-fold) and CD86 (2.15-fold) compared to ^{man}SN treatment, indicating that loaded R837 enhanced DC maturation. In the presence of US irradiation, ^{man}SNI treatment further increased the expression levels of CD80 (1.77-fold) and CD86 (1.81-fold) compared to the non-US-irradiated ^{man}SNI group, suggesting a synergistic effect between R837 and BCG-derived antigens released on promoting the proportion of mature DCs (mDCs) (Fig. 4n). In summary, ^{man}SNI generates massive ROS under US irradiation to eradicate intracellular M.tb and to promote the in situ release of M.tb-derived antigens. The ROS and R837 enhance macrophage polarization towards a pro-inflammatory phenotype, while the antigens and R837 synergistically drive DC activation, thus inducing enhanced innate and adaptive anti-TB immune response.

TBG targeting and anti-TB efficacy of ^{man}SNI in vivo

The anti-TB efficacy in vivo was investigated in the mouse model of orthotopic pulmonary tuberculosis (Fig. 5a). Firstly, the targeting effect of ^{man}SNI towards lung granulomas was validated. Following the development of characteristic TBG in the lungs on day 21 post-Mcherry-BCG infection, mice were intravenously administered with SN or ^{man}SNI. As depicted in Fig. 5b, ^{man}SNI rapidly accumulated in the lung within 6 h and reached its peak after 24 h. At this time point, the intensity of ^{man}SNI in the lung was found to be 2.19-fold higher than that of SN (Fig. 5c). Immunofluorescence assay of the lung showed ^{man}SNI co-localized well with Mcherry-BCG (Supplementary Fig. 31). To further investigate the targeting ability of ^{man}SNI towards TBG and BCG, tissue-clearing technology was employed. In contrast to traditional imaging modalities (e.g., magnetic resonance imaging, computed tomography, and fluorescence imaging), tissue-clearing technology leverages high-resolution 3D organ imaging to unveil drug distribution variations in minute tissue lesions[47]. Post chemical clarification, lung tissues underwent comprehensive 3D fluorescence imaging via light-sheet microscope (Fig. 5d). Experimental groups were administered either SN or ^{man}SNI formulations intravenously 72 h prior to euthanasia. Advanced computational reconstruction of image stacks enabled 3D visualization of Mcherry-BCG-associated granulomas, permitting simultaneous spatial mapping of granuloma lesions, SN/^{man}SNI distribution, and vascular architecture (Fig. 5e), and the results showed distinct biodistribution patterns: ^{man}SNI preferentially accumulated within granulomas, whereas SN exhibited significant pulmonary clearance (Fig. 5e, Supplementary Fig. 32 and Supplementary Movies 1–8). Notably, a strong spatial correlation between ^{man}SNI localization and Mcherry-BCG-associated granulomas distribution ($R^2 = 0.9032$) was observed (Fig. 5f). This optimized tissue clearing-based 3D imaging provides conclusive visual evidence that ^{man}SNI achieves precise targeting towards pulmonary TBG and BCG.

The anti-TB efficacy of ^{man}SNI was then evaluated against living mice (Fig. 5a). After the formation of characteristic TBG in the lung 21 days after Mcherry-BCG infection, mice were intravenously injected with saline, SN, ^{man}SN, or ^{man}SNI. Localized US-irradiation of the lung was performed at 1 day and 3 days post-injection. On day 21 after different treatments, mice were sacrificed, and their lung tissues were harvested for ex vivo fluorescence imaging (Fig. 5g and Supplementary Fig. 33) and colony formation assay (Fig. 5h, i). These results showed that in the absence of US irradiation, these semiconducting nanoparticles hardly induced any inhibitory effects against TB. Upon US irradiation, the anti-TB efficacy of ^{man}SNI was significantly higher than that of other treatments, nearly completely eliminating colonization of BCG within the lungs.

The anti-TB efficacy was further assessed using histological hematoxylin and eosin (H&E) staining. As depicted in Fig. 5j, the lung slices from the ^{man}SNI + US irradiation group exhibited significantly reduced inflammatory cellular infiltration, improved alveolar wall thickening and hemorrhage, decreased fibroblast migration and proliferation compared to the saline and ^{man}SN + US irradiation groups. However, persistent infiltration of BCG in the lungs was observed in the SN + US and ^{man}SN + US irradiation groups, as demonstrated by gold-standard acid-fast bacilli (AFB) staining for mycobacteria. In contrast, the ^{man}SNI + US irradiation group exhibited almost complete absence of BCG infiltration (Fig. 5k, l), indicating successful eradication of BCG in lungs. Additionally, throughout the treatment duration, body weight changes (Supplementary Fig. 34a) and hepatorenal function (Supplementary Fig. 34b, c) remained similar to those of normal mice. The ^{man}SNI + US irradiation group exhibited no significant histological damage in major organs, including the heart, liver, spleen, and kidneys (Supplementary Fig. 34d), thereby demonstrating its favorable biosafety profile for TB sono-immunotherapy.

Sono-immunotherapy elicits innate and adaptive immune responses in vivo

On day 7 post-treatment, lung tissues were collected from each group of mice to investigate the potential remodeling of the local immune microenvironment by ^{man}SNI-mediated sono-immunotherapy. RNA-seq analysis was employed to elucidate the genomic microenvironment of locoregional immune status. A total of over 2700 DEGs associated with ^{man}SNI + US irradiation treatment were identified compared with the saline treatment group, primarily linked to pro-inflammatory responses (Supplementary Fig. 35). KEGG pathway enrichment analysis revealed upregulation in antigen presentation and processing-related signaling pathways (shown in blue), such as TLR and NLR signaling pathways (Fig. 6a and Supplementary Fig. 36a, b). GSEA indicated significant upregulation in TLR and NF-κB-signaling pathways upon ^{man}SNI + US irradiation treatment compared to the saline group (Fig. 6b). Notably, TLR and NLR recognize intracellular pathogens, trigger macrophage activation, and subsequently initiate a series of downstream cascading inflammatory responses during M.tb infection[48]. Meanwhile, pathways associated with inflammation and immune responses (shown in green), such as the chemokine signaling pathway, Jak-stat signaling pathway, and TNF signaling pathway, were also found to be upregulated (Fig. 6a, Supplementary Fig. 36c, d). Importantly, the anti-TB pathway (shown in red) exhibited significant upregulation. The key genes, including Tnf, Tlr2, and IL1β[49], in this pathway were found to be significantly upregulated and exhibited increased expression in the heatmap and protein interaction diagram (Fig. 6c), indicating the enhanced antimicrobial activity of innate immunity. The signaling pathways associated with bacterial recognition and presentation, including TLR, MHC, and CXCR receptors (shown in blue), also demonstrated upregulation in terms of molecular function (MF) (Fig. 6d). With respect to biological processes (BP), the pathways implicated in bacterial response, immune response, and lipopolysaccharides (LPS) response were all found to be upregulated. Macrophages serving as the first line of defense against M.tb infection displayed substantial stimulation (Fig. 6e and Supplementary Fig. 37), while also successfully activating the DCs, initiating an adaptive immune response (Fig. 6f, Supplementary Fig. 38). Therefore, B cell signaling pathways (Supplementary Fig. 39) and T cell signaling pathways, including T cell-mediated immunity and CD4-positive α-β T cell

https://doi.org/10.1038/s41467-026-69420-1

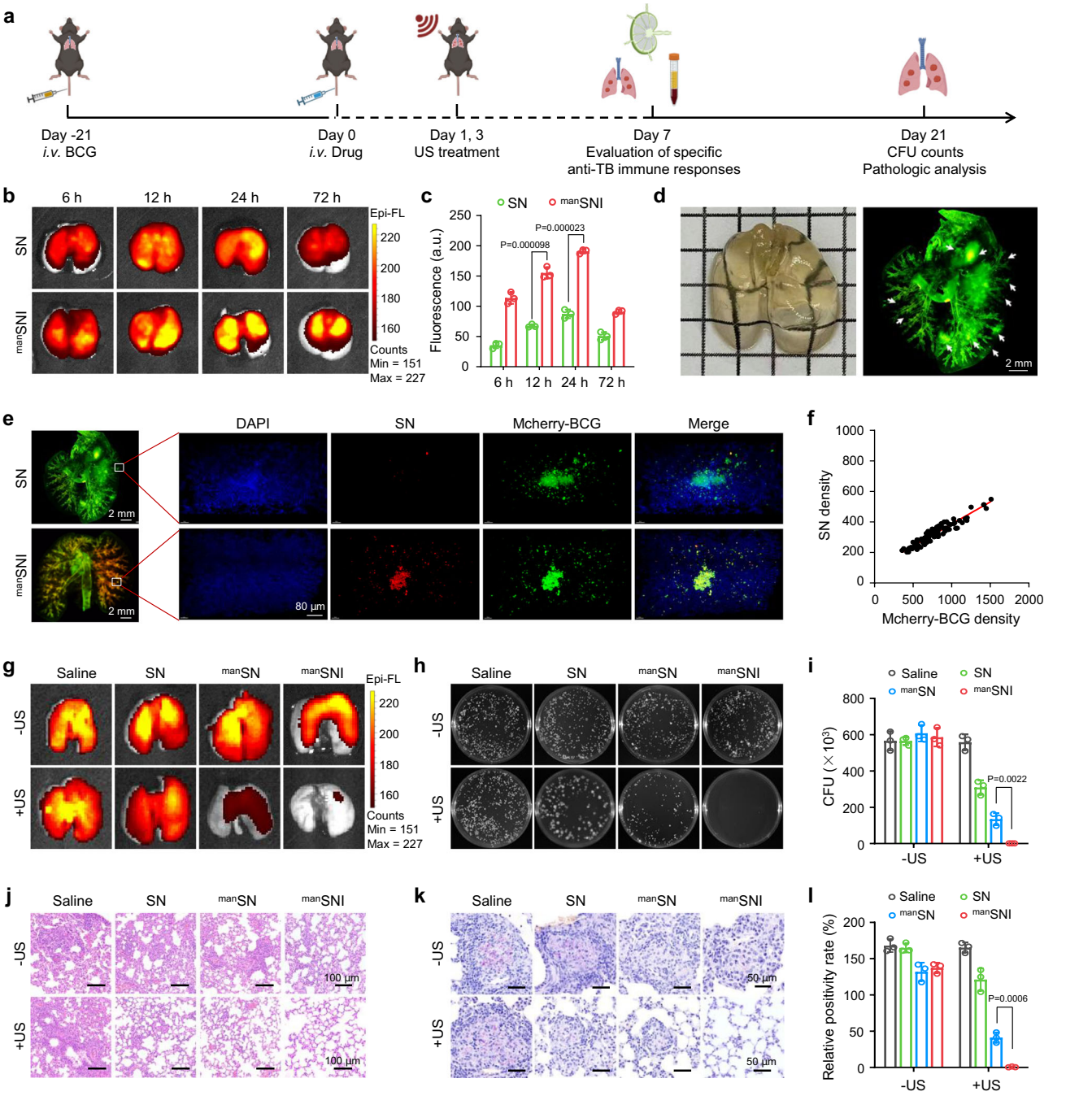

Fig. 5 | TBG targeting and anti-TB efficacy of manSNI in vivo. a Schematic illustration of manSNI-mediated anti-TB therapy in vivo. Fluorescence imaging (**b**) and quantitative analysis of fluorescence intensity (**c**) of lungs isolated from mice at different time points after the intravenous administration of SN and manSNI ($n = 3$ independent mouse). **d** Tissue-clearing and 3D fluorescence imaging of lung tissues (small arrows: TBG). **e** 3D fluorescence images of lung tissues from TBG-bearing mice after receiving SN or manSNI via intravenous administration 72 h. **f** Correlation of manSNI accumulation with Mecherry-BCG density within TBG. **g** Fluorescence images of Mcherry-BCG-infected lung tissues isolated from mice after different treatments. Treatments: mice with Mcherry-BCG-infected TB (21 days after infection) were intravenously injected with saline, SN, manSN, and manSNI. At 24 and 72 h post-injection, the entire chest area of the mice was either sonicated for 15 min (1.5 W/cm²) or not sonicated. In each group, $n = 6$ mice. Colony coating (**h**) and CFU counting (**i**) of BCG harvested from the lung tissues of TB mice on day 21 ($n = 3$ independent mouse). **j** H&E staining of the lung tissues isolated from TB mice on day 21. AFB staining (**k**) and quantification of positive area (**l**) of the lung tissues isolated from TB mice on day 21 ($n = 3$ independent mouse). For **c**, **i** and **l** data are shown as the mean ± s.d., statistical significance was calculated via one-way ANOVA with Tukey's post hoc test. Experiments were repeated independently three times with similar results in **j** and **k** and a representative result is shown for each. a.u. arbitrary units, FL fluorescence.

pathway (Supplementary Fig. 40), were also activated, suggesting a reversal of the immunosuppressive microenvironment of TBG. Most attractively, the manSNI + US irradiation treatment was able to stimulate memory T cells (Supplementary Fig. 41), which may contribute to preventing TB recurrence.

To comprehensively investigate the mechanism underlying manSNI-mediated TB sono-immunotherapy and elucidate alterations in transcriptomic profiles, immunofluorescence staining, detailed flow cytometry analysis, and cytokine level detection were performed. Firstly, macrophages within TBG underwent obvious M1 polarization

https://doi.org/10.1038/s41467-026-69420-1

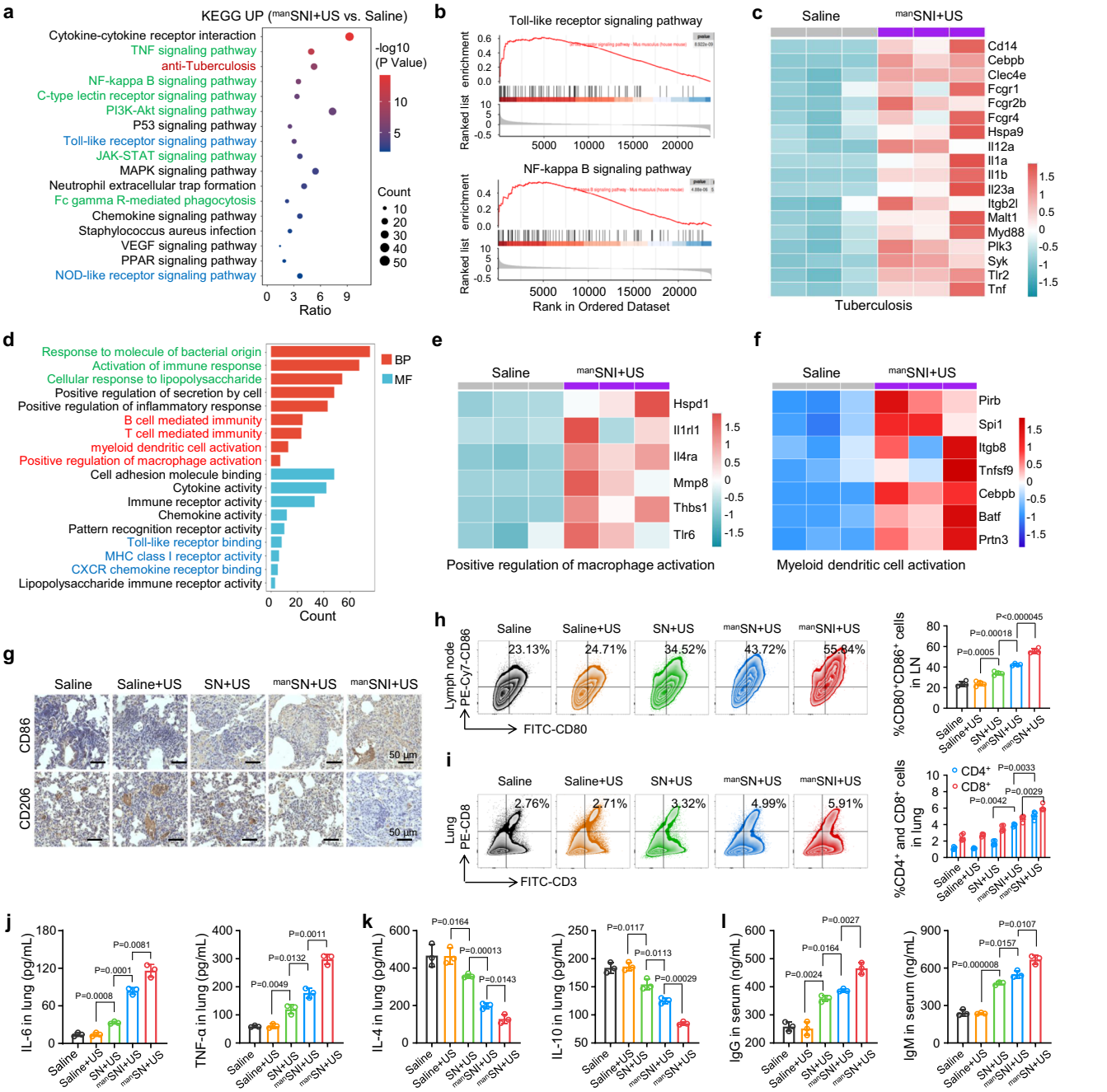

Fig. 6 | manSNI-mediated sono-immunotherapy activates robust innate and adaptive anti-TB immune responses in vivo. a KEGG enrichment analysis of the upregulated DEGs in manSNI + US irradiation treatment group ($n = 3$ independent mouse). **b** GSEA enrichment analysis of TLR signaling pathway and NF-κB signaling pathway in manSNI + US irradiation treatment group. **c** Heatmap of DEGs in the anti-tuberculosis pathway. **d** GO enrichment analysis, including BP and MF of the upregulated DEGs. Heatmap of DEGs in positive regulation of macrophage activation pathways (**e**) and myeloid dendritic cell activation pathways (**f**). BP biological process, MF molecular function. For **a**–**f**, data were presented as mean ± SD (|log2FC| > 1, $p < 0.05$). **g** Immunochemistry staining of the lung tissues within the region of granulomas isolated from mice on day 21. CD86 for M1-tpye macrophages, CD206 for M2-tpye macrophages. **h** Representative flow cytometry plots and quantification of $CD86^+$ cells after gating on $CD80^+$ cells in the lymphatic nodes on day 21 ($n = 4$ independent mouse). **i** Representative flow cytometry plots and quantification of $CD4^+$ T cells and $CD8^+$ T cells gating on $CD3^+$ cells in the lung tissues on day 21 ($n = 4$ independent mouse). IL-6, TNF-α concentrations (**j**) and IL-4, IL-10 concentrations (**k**) in the lung suspensions on day 21. **l** IgG, and IgM concentrations in the serum on day 21 ($n = 3$ independent mouse). For **h**–**l**, data are shown as the mean ± s.d., statistical significance was calculated via one-way ANOVA with Tukey's post hoc test. Experiments were repeated independently three times with similar results in **g** and a representative result is shown for each. BP biological process, MF molecular function.

following treatment with manSNI + US irradiation (Fig. 6g). Subsequently, axillary lymph nodes were collected for assessment using flow cytometry. The results demonstrated that manSNI + US irradiation treatment significantly increased the proportion of mDCs (~55.68% ± 2.31%), which was substantially higher than that observed in the saline group (~23.55% ± 2.36%) and manSN + US irradiation group (~42.35% ± 1.07%) (Fig. 6h). The high proportion of mDCs can be attributed to adjuvant stimulation and the in situ release of BCG-derived antigens from TBG during SDT. These mDCs are capable of presenting antigen information to T cells and activating them. As a result, manSNI + US irradiation treatment significantly increased the percentages of $CD4^+$ and $CD8^+$ T cells at the infectious site, with levels

2.44-fold and 4.54-fold higher than those observed following saline treatment, and 1.27-fold and 1.31-fold higher than those seen after ^{man}SN + US irradiation treatment, respectively (Fig. 6i and Supplementary Fig. 42). Concurrently, the ^{man}SNI + US irradiation group exhibited a significant elevation in IL-6 and TNF-α levels in the enzyme linked immunosorbent assay (ELISA) results of lung suspensions compared to the saline group (approximately an eightfold increase for IL-6 and fivefold increase for TNF-α) (Fig. 6j). Meanwhile, there was a corresponding decrease in IL-4 and IL-10 levels in the ^{man}SNI + US irradiation group relative to the saline group (only about one-quarter as much for IL-4; less than half as much for IL-10), indicating activation of specific T cell immune response (Fig. 6k). ELISA results for serum also demonstrated a significant increase in serum immunoglobulin G (IgG) and immunoglobulin M (IgM) levels in the ^{man}SNI + US irradiation group compared to that seen with saline treatment (about twofold increase for IgG and nearly threefold increase for IgM) (Fig. 6l), indicating effective activation of adaptive humoral immunity. Overall analyses suggest that ^{man}SNI-mediated sono-immunotherapy would activate robust innate and adaptive immune responses locally as well as systemically, which could serve as a prerequisite step towards BCG clearance by the host.

Sono-immunotherapy prevents endogenous TB relapse

The high recurrence rate, which includes endogenous relapse and exogenous reinfection, has consistently posed a significant challenge in the treatment of TB[50–52]. In the aforementioned treatment model, we have demonstrated that ^{man}SNI + US irradiation treatment exhibits remarkable therapeutic efficacy in eliminating BCG and can effectively activate adaptive immune responses, particularly immune memory. Therefore, the effectiveness of ^{man}SNI-mediated sono-immunotherapy in preventing endogenous relapse was further evaluated. The treatment protocol remained consistent with the aforementioned model. As a control group, continuous administration of the antibiotic drug rifampicin (Rif) was employed to simulate the clinical treatment strategy (i.v. Rif at 10 mg/kg every 2 days for 5 doses)[53]. Histological analysis using H&E and AFB staining confirmed that Rif treatment can almost completely eradicate BCG colonization in the lungs by day 21 (Supplementary Fig. 43). Subsequently, the evaluation period was extended to 42 days to investigate the anti-relapse efficacy of these treatments (Fig. 7a). At the conclusion of the experiment, evident TB recurrence was observed in the Rif group based on CFU analysis; BCG colonies and inflammation were still present in their lungs (Fig. 7b and Supplementary Fig. 44), as supported by H&E staining (Fig. 7c) and AFB staining results (Fig. 7d and Supplementary Fig. 45). Conversely, in mice subjected to ^{man}SNI + US irradiation treatment, TBG or inflammation was scarcely observed within lung tissues on day 42. Overall, the incidence of TB relapse was observed in 5 out of 6 mice in the Rif-treated group, whereas only 1 out of 6 mice exhibited relapse in the ^{man}SNI + US irradiation group (Fig. 7e). The above findings indicate that ^{man}SNI-mediated sono-immunotherapy can effectively prevent the relapse of the BCG-established TB model over a long-term period following treatment.

To further validate the underlying mechanisms of immune cells providing long-term protection, the contribution of memory T cell subsets in mice was evaluated. Firstly, the proportion of tissue-resident memory T cells (T_{RM}, $CD8^+CD69^+CD103^+$) in the lungs of mice on day 42 was analyzed using flow cytometry. T_{RM} level in the ^{man}SNI + US irradiation group (22.23 ± 3.15%) was about 1.68-fold higher than the Rif group (13.26 ± 1.78%) (Fig. 7f, g and Supplementary Fig. 46). This high level of T_{RM} in lung tissue is beneficial for maintaining a strong antimicrobial immune response and providing local protection against endogenous relapse[54]. Meanwhile, when exposed to bacterial antigens, the central memory T cells (T_{CM}) demonstrate the capacity for proliferation and prompt differentiation into effector cells, thereby bestowing long-term protection against residual pathogens upon the host. Subsequently, the level of T_{CM} cells in spleen tissues was analyzed. The proportion of T_{CM} cells ($CD3^+CD4^+$ $CD44^+CD62L^+$) in the ^{man}SNI + US irradiation group (73.83 ± 3.45%) was significantly higher compared to that in the Rif group (51.58 ± 1.01%) (Fig. 7h, i and Supplementary Fig. 47). Moreover, the levels of IgG and IgM (Fig. 7j, k) in the serum of mice subjected to ^{man}SNI + US irradiation (IgG: 495.7 ± 8.8 ng/mL, IgM: 668.1 ± 34.8 ng/mL) exhibited a significant increase compared to those in the Rif group (IgG: 347.3 ± 18.7 ng/mL, IgM: 558.7 ± 5.2 ng/mL), indicating that ^{man}SNI + US irradiation treatment can also elicit a long-lasting humoral immune memory response. Consequently, ^{man}SNI-mediated sono-immunotherapy could confer enduring immune memory protection, effectively preventing endogenous relapse following treatment.

Sono-immunotherapy prevents exogenous reinfection

The recurrence of TB caused by exogenous reinfection is a prevalent clinical scenario, accounting for ~6.7–18% of recurrent cases in the clinic[55,56]. Inducing long-term immune memory and facilitating rapid response to invading M.tb are crucial for protection against reinfection. Compared to Rif, considering the superior efficacy of ^{man}SNI + US irradiation in clearing BCG and activating the potent innate and adaptive anti-TB immune responses, its ability to protect against exogenous reinfection was further investigated by establishing a mouse model of secondary BCG reinfection. Following treatment with ^{man}SNI + US irradiation, mice were re-challenged with a second batch of BCG on day 21 (Fig. 8a). Memory B cells are the primary mediators of humoral immunity[57], effectively preventing reinfection by bacteria and viruses[58]. Upon subsequent exposure to the same pathogen, memory B cells exhibit a rapid and robust immune response compared to the initial encounter. Therefore, the proportion of peripheral blood memory B cells was assessed by flow cytometry analysis on day 21 prior to BCG re-challenge. Mice that were untreated after the initial infection served as the control group. The percentage of memory B cells ($CD45^+CD38^-CD19^+$) in the ^{man}SNI + US irradiation group (19.23 ± 0.82%) was significantly higher than that in the control group (5.06 ± 0.75%) (Fig. 8b, c and Supplementary Fig. 48), indicating ^{man}SNI + US irradiation can induce stronger immunogenicity and protective effect. Furthermore, following re-challenge with a second batch of BCG for one week (day 28), mice in the ^{man}SNI + US irradiation group exhibited substantially elevated levels of IgG and IgM in their serum (IgG: 937.5 ± 33.3 ng/mL, IgM: 630.2 ± 23.3 ng/mL) compared to those in the control group (IgG: 450.4 ± 17.5 ng/mL, IgM: 267.7 ± 31.9 ng/mL) (Fig. 8d, e), indicating ^{man}SNI + US irradiation induced a robust humoral immune response in mice following BCG re-challenge, leading to the production of higher levels of antibodies.

Upon re-exposure to foreign antigens, T_{CM} cells can undergo rapid proliferation and differentiation into effector memory T cells (T_{EM}, $CD3^+CD4^+CD62L^-CD44^+$) that produce crucial cytokines such as TNF-α and IL-6, thereby inducing a robust immune memory protection effect[59]. Therefore, the percentage of T_{EM} cells in the spleen was analyzed after re-challenge with the second batch of BCG for one week (day 28). Notably, the ^{man}SNI + US irradiation group exhibited a 5.02-fold higher percentage of T_{EM} cells (43.96 ± 4.72%) than that of the control group (11.65 ± 2.43%) (Fig. 8f, g). ELISA analysis revealed significantly elevated levels of IL-6 and TNF-α in the serum of mice treated with ^{man}SNI + US irradiation compared to those of the control (Fig. 8h, i). These findings suggest that ^{man}SNI + US irradiation confers long-term immune memory protection by enabling a rapid immune response to reinfection. Therefore, following re-challenge with the second batch of BCG for three weeks (day 42), four out of six mice within the ^{man}SNI + US irradiation-treated group exhibited no M.tb presence and inflammation as evidenced by CFU assay (Fig. 8j and Supplementary Fig. 49), H&E staining (Fig. 8k), and AFB staining of lung tissues (Fig. 8l and Supplementary Fig. 50), and only two out of six mice exhibited slight TBG or inflammation in lung tissue on day 42 in

https://doi.org/10.1038/s41467-026-69420-1

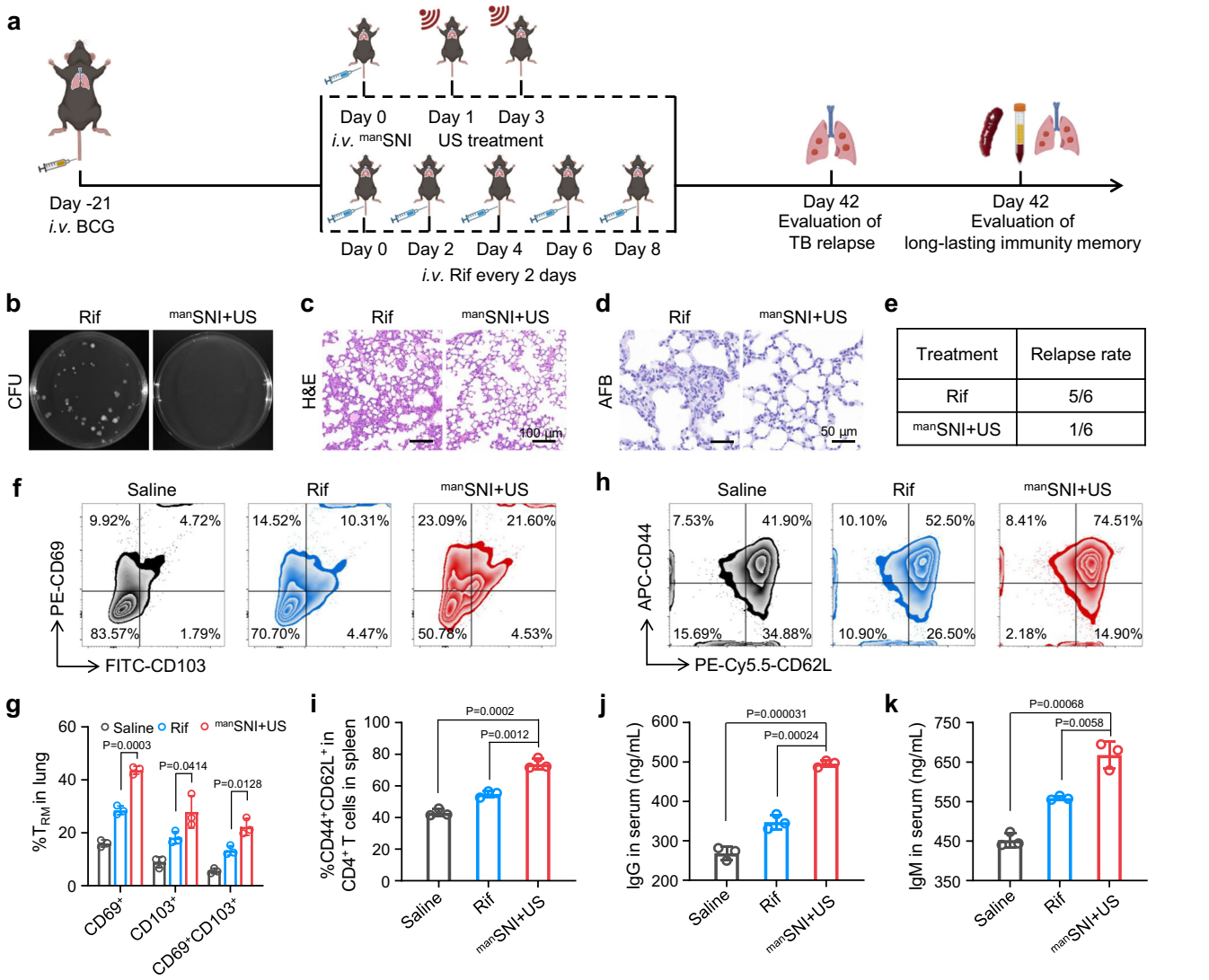

Fig. 7 | mSNI-mediated sono-immunotherapy elicits long-lasting memory immunity to prevent endogenous TB relapse. a Schematic representation of the experimental design on a mouse model of endogenous TB relapse. Rifampicin (Rif) was used as a control group for antibiotic administration. **b** Colony coating of BCG harvested from the lung tissues isolated from mice on Day 42. **c** H&E staining of the lung tissues isolated from mice on day 42. **d** AFB staining of the lung tissues isolated from mice on Day 42. **e** Rate of TB relapse in mice with Rif and mSNI + US irradiation treatment on Day 42. Representative flow cytometry plots (**f**) and quantification (**g**) of T_{RM} population ($CD8^+CD69^+CD103^+$ cells) in the lung tissues isolated from mice on Day 42 ($n = 3$ independent mouse). Representative flow cytometry plots (**h**) and quantification (**i**) of T_{CM} population ($CD62L^+CD44^+$ in $CD4^+$ T cells) in the spleen tissues isolated from mice on Day 42 ($n = 3$ independent mouse). IgG (**j**) and IgM (**k**) concentrations in the serum of mice on Day 42 ($n = 3$ independent mouse). For **g**–**k** data are shown as the mean ± s.d., statistical significance was calculated via one-way ANOVA with Tukey's post hoc test. Experiments were repeated independently three times with similar results in **c** and **d** and a representative result is shown for each.

the mSNI + US irradiation group (Fig. 8m). Thus, mSNI-mediated sono-immunotherapy also elicited robust immune memory to effectively prevent reinfection by BCG.

Discussion

In summary, by employing bioinformatic analyses to investigate the immune microenvironment within clinical NTBG, TBG, and peripheral blood from drug-resistant vs. drug-sensitive and recurrent vs. non-recurrent TB patients, we have identified significant immune imbalances and a pronounced inclination towards suppression of innate immune response marked by downregulated TLR and NF-κB signaling pathways in macrophages and DCs, alongside elevated negative immune regulation of B cell and T cell activities. Based on these findings, we developed an organic semiconducting nano-immunostimulants (mSNI) system equipped with a mannose warhead for highly targeted and precise TB sono-immunotherapy and recurrence prevention. Following systemic administration, mSNI demonstrated not only a 2.19-fold higher accumulation in the lungs compared to SN but also effectively eliminated M.tb (BCG and H37Ra) within lung granulomas and macrophages through localized ultrasonic irradiation, resulting in a bacterial death rate exceeding 99%. Additionally, the generated ROS can activate macrophages toward a pro-inflammatory state in combination with R837. Meanwhile, the in situ release of M.tb-derived antigens and R837 from macrophages could synergistically promote DC maturation. These effects collectively trigger potent innate and adaptive anti-TB immune responses at the infection site, effectively reversing the immunosuppressive microenvironment of TBG. This included a pronounced macrophage polarization towards M1 phenotype and a substantial increase in the proportion of mDCs (~55.68% compared to ~23.50% in the saline group). Moreover, it markedly enhanced the proportions of $CD4^+$ T cells by 2.44-fold and $CD8^+$ T cells by 4.54-fold compared to the saline

https://doi.org/10.1038/s41467-026-69420-1

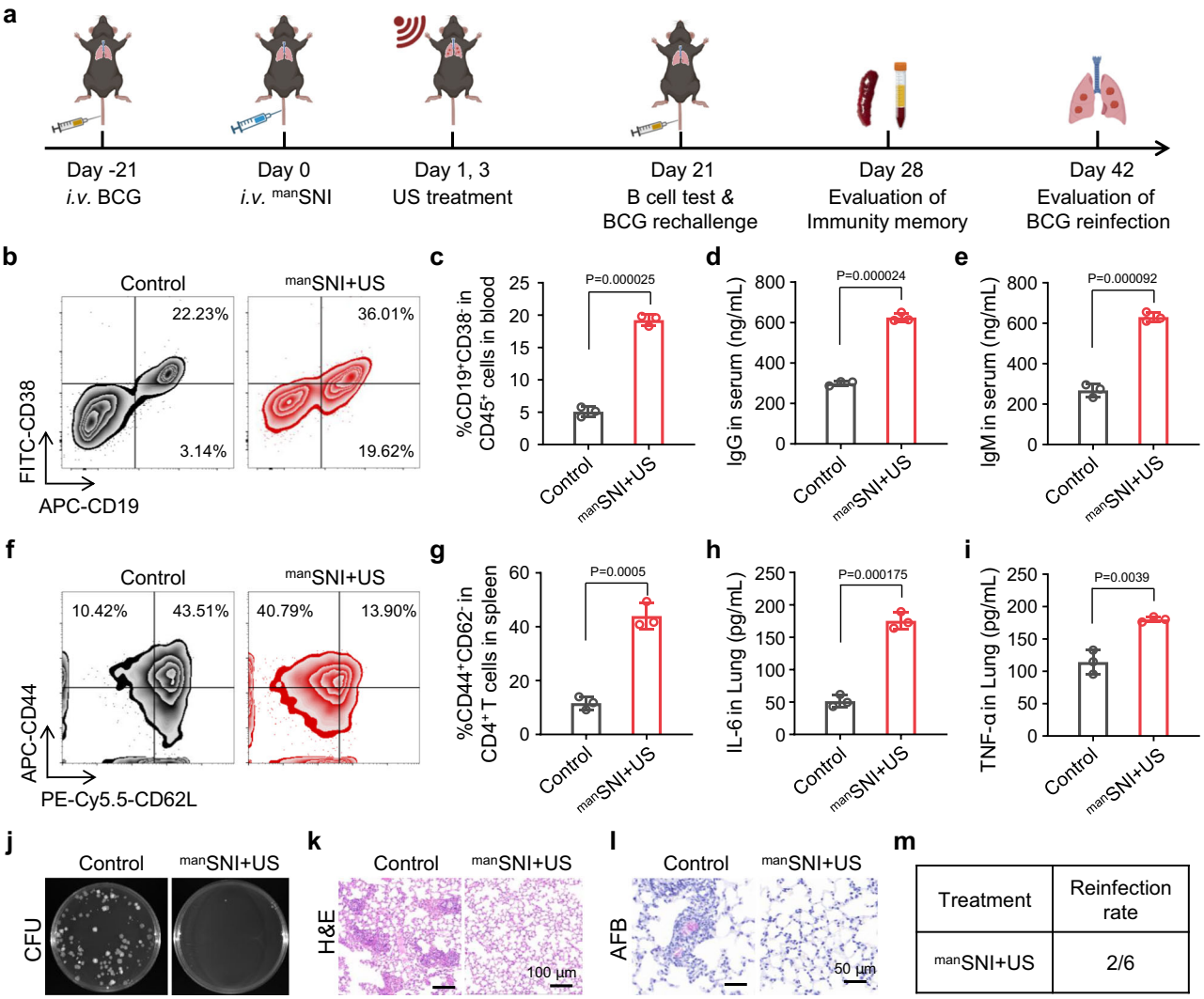

Fig. 8 | mSNI-mediated sono-immunotherapy prevents exogenous reinfection. a Schematic representation of the experimental design on a mouse model of BCG re-challenged. Representative flow cytometry plots (**b**) and quantification (**c**) of memory B cells ($CD45^+CD19^+CD38^-$) after gating on $CD45^+$ cells in the blood of mice prior to BCG re-challenge on day 21 ($n = 3$ independent mouse). IgG (**d**) and IgM (**e**) concentrations in the serum of re-challenged mice on day 28 ($n = 3$ independent mouse). Representative flow cytometry plots (**f**) and quantification (**g**) of T_{EM} population ($CD62L^-CD44^+$ in $CD4^+$ T cells) in the spleen tissues isolated from rechallenged mice on day 28 ($n = 3$ independent mouse). IL-6 (**h**) and TNF-α (**i**) concentrations in the serum of reinfection mice on day 28 ($n = 3$ independent mouse). **j** Colony coating of BCG in the lung tissues isolated from rechallenged mice on day 42. **k** H&E staining of the lung tissues isolated from rechallenged mice on Day 42. **l** AFB staining of the lung tissues isolated from rechallenged mice on day 42. **m** Rate of BCG reinfection on day 42 ($n = 3$ independent mouse). For **c**–**e** and **g**–**i** data are shown as the mean ± s.d., statistical significance was calculated via one-way ANOVA with Tukey's post hoc test. Experiments were repeated independently three times with similar results in **k** and **l** and a representative result is shown for each.

group. Furthermore, treatment with mSNI + US irradiation induced long-term immune memory responses, which enhanced the proportions of peripheral blood memory B cells by 3.79-fold and effector memory T cells by 5.02-fold compared to the control group, thus effectively preventing TB recurrence including endogenous relapse (relapse rate of 17% compared to 83% in the rifampicin group) as well as exogenous reinfection (reinfection rate of 33%). The present innovative sono-immunotherapy strategy synergistically amalgamated localized eradication of M.tb with robust activation of immunological responses, thereby resulting in significantly augmented treatment efficacy and effectively averting TB recurrence (Fig. 9).

The granulomas immune microenvironment-guided sono-immunotherapy strategy we designed successfully integrates the dual mechanisms of pathogen clearance and immune activation, providing an integrated "clear-prevent" solution for TB treatment, particularly suitable for recurrent TB. Moreover, ultrasound, a widely used clinical physical modality, enables non-invasive, high-penetration, precise intervention with excellent clinical compatibility. Therefore, this mSNI-mediated sono-immunotherapy strategy demonstrates clinical translational potential for TB treatment. Despite the promising findings, this study also has several limitations. First, due to biosafety constraints, the anti-TB efficacy was validated using attenuated strains (BCG and H37Ra) rather than virulent M.tb strains such as the H37Rv strain or clinical isolates. Clinical M.tb strains exhibit distinct pathogenicity, immune evasion mechanisms, and cell wall components, which may affect the translatability of our findings. Second, the impact of distinct M.tb strain lineages (e.g., the Beijing family vs. non-Beijing strains) on the immune microenvironment of drug-resistant and drug-sensitive patients was overlooked. Due to the lack of strain typing data in the GEO datasets, we were unable to dissect whether strain-specific characteristics affect the immune differences between drug-resistant and drug-sensitive patients. Third, the mouse model used in this study may not fully recapitulate the complexity of human TB, including granuloma structure and immune-cell diversity. Fourth, the relatively

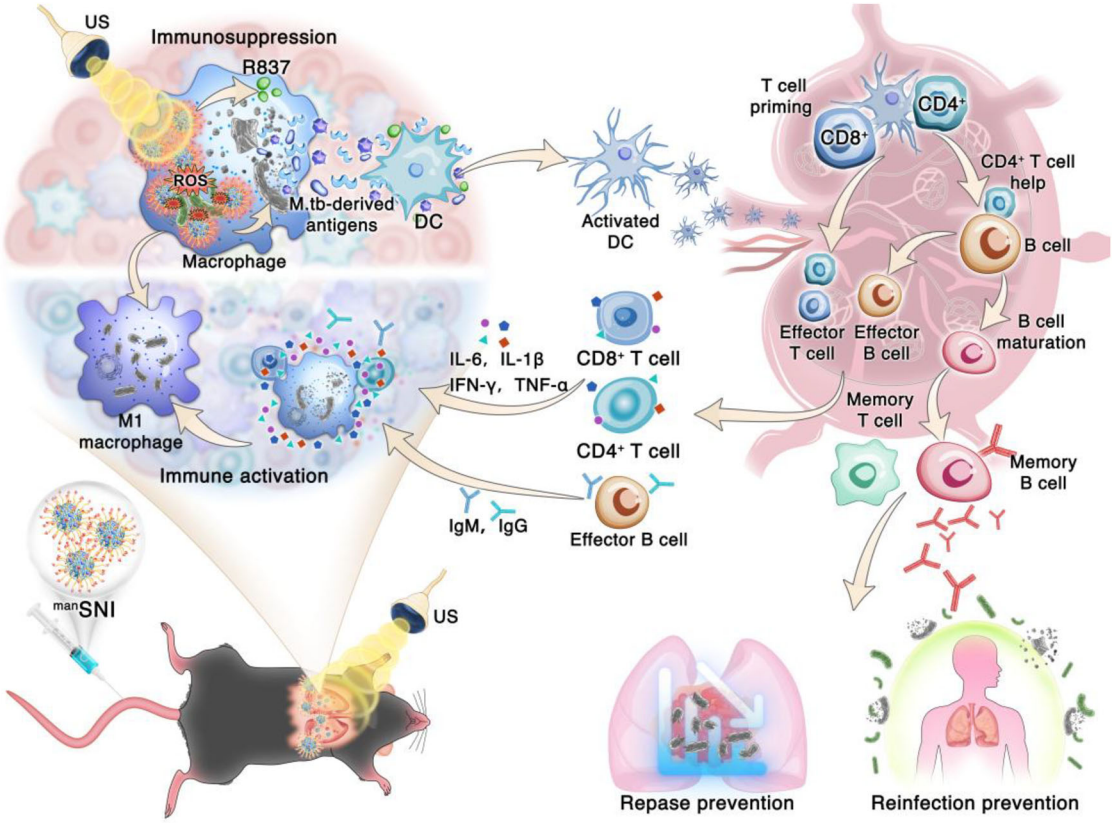

Fig. 9 | ^{man}SNI-mediated TB sono-immunotherapy. ^{man}SNI targets TBG to selectively kill M.tb in macrophages, triggers potent innate and adaptive anti-TB immune responses to reverse the immunosuppression of TBG, achieving efficient treatment of TB and prevention of recurrence.

small sample sizes ($n = 3$–4 for in vitro assays, $n = 6$ for in vivo experiments) may limit statistical power. Finally, the US devices used in small-animal studies differ substantially from clinical systems in parameter ranges and tissue compatibility. To further enhance the translational relevance of this strategy, future studies will involve collaborations with accredited laboratories to evaluate the efficacy of ^{man}SNI-mediated sono-immunotherapy against a panel of clinically relevant M.tb strains. Additionally, we plan to extend the preclinical assessment to large animal models, including guinea pigs and non-human primates, which more accurately recapitulate the pathological characteristics of human TB. These studies will employ appropriately expanded group sizes ($n \geq 10$ per group) to ensure robust statistical power and will systematically optimize ultrasound parameters—including intensity, duration, and frequency—to align with the operational specifications of clinical ultrasound systems. Overall, our study presents a groundbreaking approach for TB treatment guided by the immune microenvironment of TBG, and proposes a promising direction for the development of tailored surveillance systems and therapeutic strategies against other highly pathogenic infections.

Online content

Any methods, additional references, Nature Portfolio reporting summaries, source data, extended data, supplementary information, acknowledgements, peer review information; details of author contributions and competing interests; and statements of data and code availability are available online.

Methods

Preparation and characterization ^{man}SNI

The preparation and characterization of ^{man}SNI are placed in the Supplementary Information.

M.tb strains and culture

Bacillus Calmette-Guultu strains, with or without fluorescent reporter gene constructs, namely BCG, GFP-BCG, and Mcherry-BCG, were utilized in this study. The cultivation of BCG was conducted in 7H9 medium supplemented with 10% oleic albumin dextrose catalase (OADC) at a temperature of 37 °C. GFP-BCG was cultured in 7H9 broth medium supplemented with kanamycin at a concentration of 30 μg/mL. Similarly, Mcherry-BCG was grown in 7H9 broth medium containing kanamycin at the same concentration. The attenuated strain of M.tb H37Ra (ATCC25177) was grown in Middlebrook 7H10 solid medium supplemented with 10% oleic acid–albumin–dextrose–catalase enrichment (BD Difco Laboratories). The in vitro and in vivo experiments associated with Mycobacterium were conducted in a biosafety level II laboratory located at Southern Medical University. All the strains were purchased from Shanghai Jingnuo Biotechnology Co., Ltd.

^{man}SNI targets macrophages and intracellular M.tb

To target macrophages, Raw264.7 cells were seeded at a density of 1×10^6 cells/well in confocal dishes overnight. Subsequently, the SN and ^{man}SNI (at a concentration of 100 μg/mL based on SN) were added to the confocal dishes. After 12 h, the cells were washed three times with PBS and fixed in 4% paraformaldehyde for 15 min. Lysosomal probes were used to label the lysosomes of Raw264.7 cells following the manufacturer's instructions. Cell nuclei were stained using an anti-fluorescence quencher containing DAPI. Finally, images were acquired using a confocal laser scanning microscope (FV3000, OLYMPUS).

The intracellular infection model was modified based on previous methods[60]. To establish an intracellular bacterial model for targeting BCG within macrophages, Raw264.7 cells were seeded at a density of 1×10^6 cells/well in confocal dishes and incubated overnight. Subsequently, the cells were infected with GFP-BCG for 3 h, followed by

removal of the medium and three washes with PBS. Fresh medium was then added to the cells, which were subsequently treated with SN and ^{man}SNI (at a concentration of 100 μg/mL based on SN). After 24 h of treatment, the medium was removed, and the cells were washed three times with PBS before fixation using 4% paraformaldehyde for 15 min. Finally, DAPI staining was performed, and images were captured using a confocal laser scanning microscope (FV3000, OLYMPUS).

Effectiveness of SN, ^{man}SN, and ^{man}SNI in killing intracellular M.tb

Raw264.7 cells were seeded at a density of 1×10^6 cells/well in confocal dishes overnight. Subsequently, the cells were infected with BCG (MOI = 10). After 3 h, the uninfected cells were washed with PBS to remove bacteria. Following this, the cells were treated with SN, ^{man}SN, and ^{man}SNI (at a concentration of 100 μg/mL based on SN). After 12 h, the drug-containing medium was replaced with fresh medium. The US-irradiation groups (PBS, SN, ^{man}SN and ^{man}SNI) underwent US irradiation using a small-animal sonicator (Intelect Portable Ultrasonic Therapeutic Instrument) for 10 min at an intensity of 1.5 W/cm^2; whereas the non-US-irradiation groups (PBS, SN, ^{man}SN, and ^{man}SNI) remained untreated. The cells were then incubated at 37 °C with 5% CO_2 for an additional 24 h. Finally, cell lysis was performed using 0.1% Triton X-100 for 15 min followed by dilution with PBS to obtain specific concentrations of cell lysates, which were subsequently inoculated on Middlebrook's solid medium (7H10). The plates were incubated at 37 °C for a period of time ranging from 21 to 30 days before counting and recording colony numbers.

Phenotyping cultures of macrophages and BMDCs in vitro

To evaluate the activation of macrophages by ^{man}SNI, an intracellular infection model of BCG was established following the aforementioned protocol. Subsequently, cells were treated with PBS, SN, ^{man}SN, and ^{man}SNI (at a concentration of 100 μg/mL based on SN). After 12 h, the medium was replaced with fresh medium. The US-irradiation groups underwent sonication using a small animal sonicator for 10 min (at a power density of 1.5 W/cm^2). The non-US-irradiation groups remained untreated. Following this treatment regimen, the samples were incubated at 37 °C in a CO_2 incubator for an additional 24 h. The culture medium was collected to measure the expression levels of inflammatory cytokines (IL-6 and TNF-α) using enzyme-linked immunosorbent assay (ELISA), while flow cytometry analysis was performed on the collected cells to assess their differentiation.

The macrophages were processed using the aforementioned method. Subsequently, BMDCs were isolated following established protocols[61]. BMDCs were then seeded into transwell plates at a density of 50,000 cells per well and cultured overnight. Afterwards, the cells were collected and subjected to flow cytometry analysis in accordance with the manufacturer's recommendations to evaluate the maturation status of BMDCs.

Detailed ultrasound parameters used in animal experiments

The ultrasound device used in this study was the Intelect Portable Ultrasonic Therapeutic Instrument (Chattanooga Group, USA) equipped with a 2776 transducer, operating at a fixed frequency of 1 MHz with an adjustable power density range of 0.5–3.0 W/cm^2.

Parameter calibration and verification

Before the experiments, ultrasound intensity was calibrated using a hydrophone (HNR-0500, Onda Corporation, USA) in a simulated body fluid environment at 37 °C. The calibration was performed at a vertical distance of ~1 cm between the ultrasound probe and the target tissue (mouse lung), consistent with the irradiation distance during the treatment. This ensured that the nominal intensity (1.5 W/cm^2) matched the actual intensity acting on the lesions.

During lung irradiation, the thickness of the acoustic couplant layer (2–5 mm) between the probe and the skin was kept consistent across animals to minimize variability in intensity attenuation. The US-irradiation groups received ultrasound irradiation using a small-animal sonicator for 10 min at 24 and 72 h post-injection, with a duty cycle of 50% and continuous-wave irradiation mode, at a power density of 1.5 W/cm^2.

Anti-TB efficacy of ^{man}SNI + US irradiation treatment in vivo

The animal experimental protocol was reviewed by the Experimental Animal Ethics Committee of Guangdong Medical Laboratory Animal Center and complied with the relevant ethical norms (approval number C202401-2). Mice were raised in a specific pathogen-free (SPE) grade animal laboratory. Mice were housed at light/dark cycle: 12 h/12 h; temperature: 22–24 °C; humidity: 50 ± 5%. A mouse tuberculosis model was established by nebulized inhalation of Mcherry-BCG (10^7 CFU/mL, 100 μL). Intravenous injections of saline, SN, ^{man}SN, and ^{man}SNI solutions (based on an SN concentration of 10 mg/kg) were administered 21 days after infection. The US-irradiation groups underwent ultrasound irradiation using a small animal sonicator for 10 min at 24 and 72 h post-injection with a power density of 1.5 W/cm^2. The non-US-irradiation groups remained untreated. After another 21 days had elapsed from the injection time point, the mice were euthanized to collect their lungs for subsequent analysis. A portion of the lung tissue was imaged using a small animal in vivo imaging system to quantify the fluorescence intensity emitted by Mcherry-BCG as an indicator of bacterial load in the lungs. Simultaneously, another portion was subjected to colony-forming unit determination assay. Additionally, lung tissue sections were prepared for H&E staining along with immunohistochemical and AFB staining.

In vivo activation of immune responses by ^{man}SNI treatment

A mouse tuberculosis model was established as described above. After one week of treatment, the lungs, lymph nodes, and spleens were collected from the mice. Subsequently, these organs were cut into small pieces and enzymatically degraded for 1 h at 37 °C using 1 mg/mL Collagenase IV. The resulting suspensions were then passed through 70 μm cell filters to obtain individual cell suspensions after removing erythrocytes with erythrocyte lysate (Gibco). To analyze the composition of immune cells, the obtained cell suspensions were incubated with CD16/32 for 10 min followed by staining with fluorescent antibodies (FITC-CD103, PE-CD69, APC-CD8, PE-Cy5.5-CD62L, APC-CD44, FITC-CD4, PE-CD3, PE-CD45, APC-CD19, and FITC-CD38) on ice for 30 minutes. The same staining protocol used in vitro was applied for CD206 staining as well. Cytokine levels (IL-6, TNF-α, IL-4, and IL-10) and serum antibody levels (IgM and IgG) in the lungs were determined using ELISA kits according to the manufacturer's instructions. For RNA-seq analysis, total RNA was extracted using Trizol reagent and subsequently subjected to RNA-seq analysis conducted by BGI Genomics.

Prevention of TB relapse

A mouse TB model was established using the aforementioned method, and mice were treated with Rif and ^{man}SNI. Rifampicin (Rif) was dissolved in dimethyl sulfoxide (DMSO) (100 mg Rif/mL) and diluted with saline to a final DMSO concentration of 1% before use. Mice in the Rif control group received intravenous injection of Rif at 10 mg/kg (0.1 mL per mouse) every 2 days for a total of 5 doses. ^{man}SNI solutions ([SN] = 10 mg/kg) were administered 21 days after infection. US irradiation was applied using a small animal sonicator for 10 min at 24 and 72 h post-injection of ^{man}SNI with a power density of 1.5 W/cm^2. After a period of 42 days, lung, spleen, and blood samples were collected and processed following the protocol described in "In vivo activation of immune effects by ^{man}SNI. Flow analysis was conducted to assess the induction of long-lasting immunity in mice. Simultaneously, lung tissues from mice were collected for CFU assay as well as H&E staining and AFB staining to evaluate tuberculosis recurrence.

Prevention of BCG reinfection

A mouse TB model was established as previously described, and mice were treated with ^{man}SNI + US. After 21 days, a portion of the spleen and lymph nodes was collected and processed according to the method "In vivo activation of immune effects by ^{man}SNI. Flow cytometry analysis was performed to determine the composition of immune cells prior to secondary BCG reinfection. Simultaneously, another group of mice was used for reinfection experiments where BCG (10^7 CFU/mL, 100 µL) was nebulized and inhaled. After 7 days, a portion of spleens and lymph nodes was collected and processed using the method "In vivo activation of immune effects by ^{man}SNI for flow cytometry analysis to determine the composition of immune cells after reinfection. Cytokine levels (IL-6 and TNF-α) as well as serum antibody levels (IgM and IgG) were measured using ELISA kits following the manufacturer's instructions. Finally, at indicated time points (21 days after reinfection), mice were euthanized, and lung tissues were collected for evaluation of bacterial load through histopathological sections and acid-fast staining.

Data analysis

The quantitative data were presented as the mean ± s.d. All experiments were performed with a minimum of three replicates. Statistical analysis between the two groups was conducted using two-sided unpaired *t*-tests. One-way ANOVA followed by post-hoc correction was employed for multiple comparisons. A probability value <0.05 ($P < 0.05$) was considered statistically significant[62].

Reporting summary

Further information on research design is available in the Nature Portfolio Reporting Summary linked to this article.

Data availability

The single-cell RNA sequencing data for the tuberculosis (TB) group were obtained by downloading public data from NCBI GEO (GSE192483). Sarcoidosis-like tuberculous granuloma samples were sourced from GEO (GSE192456), while lung control samples were obtained from GEO (GSE135893). Additionally, the transcriptome sequencing datasets used in this study for the peripheral blood of tuberculosis recurrence and cured groups originated from GEO (GSE67589). The transcriptome sequencing datasets for drug-resistant and non-drug-resistant TB patients were sourced from GEO (GSE147689). The data files of protein identification by LC–MS/MS have been deposited in the ProteomeXchange database under the accession number IPX0014557000 (http://proteomecentral.proteomexchange.org/cgi/GetDataset?ID = PXD071692). The cell RNA-seq data files have been deposited in the National Library of Medicine under the Accession ID PRJNA1378147. Source data are provided with this paper. Source data for Figs. 3–8 are available in separate source data files for Figs. 3c–i, l, 4d, f, h, j–n, 5c, f, i, l, 6h–l, 7f–k, and 8b–i, respectively. Source supplementary data are available in supplementary files for Supplementary Figs. 17, 18, 19b, 20a–c, 21b, c, 22, 23b, 24b, 25b, 26, 27, 33, 34a–c, 42 and 44–50, respectively. Source data are provided with this paper. Other datasets generated during and/or analyzed during the current study are available from the corresponding author upon reasonable request. Source data are provided with this paper.

References

1. *Global Tuberculosis Report 2024* (World Health Organization, 2024).
2. van Doorn, C. L. R. et al. Transcriptional profiles predict treatment outcome in patients with tuberculosis and diabetes at diagnosis and at two weeks after initiation of anti-tuberculosis treatment. *EBioMedicine* **82**, 104173 (2022).
3. Helaine, S., Conlon, B. P., Davis, K. M. & Russell, D. G. Host stress drives tolerance and persistence: the bane of anti-microbial therapeutics. *Cell Host Microbe* **32**, 852–862 (2024).
4. Ramakrishnan, L. Revisiting the role of the granuloma in tuberculosis. *Nat. Rev. Immunol.* **12**, 352–366 (2012).
5. Caño-Muñiz, S., Anthony, R., Niemann, S. & Alffenaar, J. C. New approaches and therapeutic options for *Mycobacterium tuberculosis* in a dormant state. *Clin. Microbiol. Rev.* **31**, e00060–17 (2018).
6. van Rie, A. et al. Exogenous reinfection as a cause of recurrent tuberculosis after curative treatment. *N. Engl. J. Med.* **341**, 1174–1179 (1999).
7. Verver, S. et al. Rate of reinfection tuberculosis after successful treatment is higher than rate of new tuberculosis. *Am. J. Respir. Crit. Care Med.* **171**, 1430–1435 (2005).
8. Youn, H. M. et al. Risk factors associated with tuberculosis recurrence in South Korea determined using a nationwide cohort study. *PLoS ONE* **17**, e0268290 (2022).
9. Abrahams, K. A. et al. DprE2 is a molecular target of the anti-tubercular nitroimidazole compounds pretomanid and delamanid. *Nat. Commun.* **14**, 3828 (2023).
10. Wallis, R. S., O'Garra, A., Sher, A. & Wack, A. Host-directed immunotherapy of viral and bacterial infections: past, present and future. *Nat. Rev. Immunol.* **23**, 121–133 (2023).
11. Vekemans, J. et al. Preferred product characteristics for therapeutic vaccines to improve tuberculosis treatment outcomes: key considerations from World Health Organization consultations. *Vaccine* **38**, 135–142 (2020).
12. Li, B. et al. Photothermal therapy of tuberculosis using targeting pre-activated macrophage membrane-coated nanoparticles. *Nat. Nanotechnol.* **19**, 834–845 (2024).
13. Wang, H. et al. NIR-II AIE luminogen-based erythrocyte-like nanoparticles with granuloma-targeting and self-oxygenation characteristics for combined phototherapy of tuberculosis. *Adv. Mater.* **36**, 2406143 (2024).
14. Wang, W. et al. Biosafety materials for tuberculosis treatment. *Biosaf. Health.* **4**, 258–268 (2022).
15. Suman, S. K., Chandrasekaran, N. & Priya Doss, C. G. Micro-nanoemulsion and nanoparticle-assisted drug delivery against drug-resistant tuberculosis: recent developments. *Clin. Microbiol. Rev.* **36**, e0008823 (2023).
16. Wang, L. et al. Single-cell RNA-sequencing reveals heterogeneity and intercellular crosstalk in human tuberculosis lung. *J. Infect.* **87**, 373–384 (2023).
17. Gideon, H. P. et al. Multimodal profiling of lung granulomas in macaques reveals cellular correlates of tuberculosis control. *Immunity* **55**, 827–846.e810 (2022).
18. Cliff, J. M. et al. Excessive cytolytic responses predict tuberculosis relapse after apparently successful treatment. *J. Infect. Dis.* **213**, 485–495 (2016).
19. Chai, Q., Wang, L., Liu, C. H. & Ge, B. New insights into the evasion of host innate immunity by *Mycobacterium tuberculosis*. *Cell. Mol. Immunol.* **17**, 901–913 (2020).
20. McCaffrey, E. F. et al. The immunoregulatory landscape of human tuberculosis granulomas. *Nat. Immunol.* **23**, 318–329 (2022).
21. Nagai, Y. et al. Requirement for MD-1 in cell surface expression of RP105/CD180 and B-cell responsiveness to lipopolysaccharide. *Blood* **99**, 1699–1705 (2002).
22. Zhuang, L., Yang, L., Li, L., Ye, Z. & Gong, W. *Mycobacterium tuberculosis*: immune response, biomarkers, and therapeutic intervention. *MedComm* **5**, e419 (2024).
23. Hwang, A. A. et al. pH-responsive isoniazid-loaded nanoparticles markedly improve tuberculosis treatment in mice. *Small* **11**, 5066–5078 (2015).

24. Tiberi, S. et al. Tuberculosis: progress and advances in development of new drugs, treatment regimens, and host-directed therapies. *Lancet Infect. Dis.* **18**, 183–198 (2018).
25. Piksa, M. et al. The role of the light source in antimicrobial photodynamic therapy. *Chem. Soc. Rev.* **52**, 1697–1722 (2023).
26. Son, S. et al. Multifunctional sonosensitizers in sonodynamic cancer therapy. *Chem. Soc. Rev.* **49**, 3244–3261 (2020).
27. Ouyang, J. et al. Ultrasound mediated therapy: Recent progress and challenges in nanoscience. *Nano Today* **35**, 100949 (2020).
28. Li, Y. et al. Nanosensitizer-mediated augmentation of sonodynamic therapy efficacy and antitumor immunity. *Nat. Commun.* **14**, 6973 (2023).
29. Li, J. et al. Precision cancer sono-immunotherapy using deep-tissue activatable semiconducting polymer immunomodulatory nanoparticles. *Nat. Commun.* **13**, 4032 (2022).
30. Li, J. & Pu, K. Development of organic semiconducting materials for deep-tissue optical imaging, phototherapy and photoactivation. *Chem. Soc. Rev.* **48**, 38–71 (2019).
31. Pu, K. et al. Semiconducting polymer nanoparticles as photoacoustic molecular imaging probes in living mice. *Nat. Nanotechnol.* **9**, 233–239 (2014).
32. Tang, D. et al. Self-sacrificially degradable pseudo-semiconducting polymer nanoparticles that integrate NIR-II fluorescence bioimaging, photodynamic immunotherapy, and photo-activated chemotherapy. *Adv. Mater.* **34**, e2203820 (2022).
33. Li, W., Liang, M., Qi, J. & Ding, D. Semiconducting polymers for cancer immunotherapy. *Macromol. Rapid Commun.* **44**, e2300496 (2023).
34. Xu, C. et al. Nanoparticles with ultrasound-induced afterglow luminescence for tumour-specific theranostics. *Nat. Biomed. Eng.* **7**, 298–312 (2023).
35. He, S. et al. A semiconducting iron-chelating nano-immunomodulator for specific and sensitized sono-metallo-immunotherapy of cancer. *Angew. Chem. Int. Ed. Engl.* **62**, e202310178 (2023).
36. Li, F. et al. Organic semiconducting sono-metallo-detonated immunobombs for ultrasensitized domestication of immunosuppressive cells. *Nano Lett.* **24**, 7340–7349 (2024).
37. Sparks, I. L. et al. Lipoarabinomannan mediates localized cell wall integrity during division in mycobacteria. *Nat. Commun.* **15**, 2191 (2024).
38. Kang, P. B. et al. The human macrophage mannose receptor directs *Mycobacterium tuberculosis* lipoarabinomannan-mediated phagosome biogenesis. *J Exp. Med.* **202**, 987–999 (2005).
39. Behr, M. A. B. C. G. different strains, different vaccines?. *The Lancet Infect. Dis.* **2**, 86–92 (2002).
40. Akira, S., Uematsu, S. & Takeuchi, O. Pathogen recognition and innate immunity. *Cell* **124**, 783–801 (2006).
41. Narayan, R. et al. Immunomodulation by imiquimod in patients with high-risk primary melanoma. *J. Investig. Dermatol.* **132**, 163–169 (2012).
42. Wang, Y. et al. Small-molecule modulators of toll-like receptors. *Acc. Chem. Res.* **53**, 1046–1055 (2020).
43. West, A. P. et al. TLR signalling augments macrophage bactericidal activity through mitochondrial ROS. *Nature* **472**, 476–480 (2011).
44. Panda, S. et al. Identification of differentially recognized T cell epitopes in the spectrum of tuberculosis infection. *Nat. Commun.* **15**, 765 (2024).
45. Musvosvi, M. et al. T cell receptor repertoires associated with control and disease progression following *Mycobacterium tuberculosis* infection. *Nat. Med.* **29**, 258–269 (2023).
46. Liang, J. et al. Engineering versatile nanomedicines for ultrasonic tumor immunotherapy. *Adv. Sci.* **11**, e2305392 (2024).
47. Rong, Z., Ertürk, A., Tang, Y. & Mai, H. Tissue clearing and its application in nanoparticle development. *Small* **21**, 2410032 (2025).
48. Liu, T. et al. Blocking triggering receptor expressed on myeloid cells-1 attenuates lipopolysaccharide-induced acute lung injury via inhibiting NLRP3 inflammasome activation. *Sci. Rep.* **6**, 39473 (2016).
49. Kaufmann, S. H. E., Dorhoi, A., Hotchkiss, R. S. & Bartenschlager, R. Host-directed therapies for bacterial and viral infections. *Nat. Rev. Drug Discov.* **17**, 35–56 (2018).
50. Hermans, S. M. et al. High rates of recurrent tuberculosis disease: a population-level cohort study. *Clin. Infect. Dis.* **72**, 1919–1926 (2021).
51. Panjabi, R., Comstock, G. W. & Golub, J. E. Recurrent tuberculosis and its risk factors: adequately treated patients are still at high risk. *Int. J. Tuberc. Lung Dis.* **11**, 828–837 (2007).
52. Lambert, M. L. et al. Recurrence in tuberculosis: relapse or reinfection? *The Lancet Infect. Dis.* **3**, 282–287 (2003).
53. Sterling, T. R. et al. Three months of rifapentine and isoniazid for latent tuberculosis infection. *N. Engl. J. Med.* **365**, 2155–2166 (2011).
54. Schenkel, J. M. & Masopust, D. Tissue-resident memory T cells. *Immunity* **41**, 886–897 (2014).
55. Barnes, P. F. & Cave, M. D. Molecular epidemiology of tuberculosis. *N. Engl. J. Med.* **349**, 1149–1156 (2003).
56. Chiang, C. Y. & Riley, L. W. Exogenous reinfection in tuberculosis. *The Lancet Infect. Dis.* **5**, 629–636 (2005).
57. Wu, M. et al. Innervation of nociceptor neurons in the spleen promotes germinal center responses and humoral immunity. *Cell* **187**, 2935–2951.e19 (2024).
58. Lyashchenko, K. P., Vordermeier, H. M. & Waters, W. R. Memory B cells and tuberculosis. *Vet. Immunol. Immunopathol.* **221**, 110016 (2020).
59. Hu, Z. et al. Extracellular vesicle-inspired therapeutic strategies for the COVID-19. *Adv. Healthc. Mater.* **13**, e2402103 (2024).
60. Wang, W. et al. Antibiotic-loaded lactoferrin nanoparticles as a platform for enhanced infection therapy through targeted elimination of intracellular bacteria. *Asian J. Pharm. Sci.* **19**, 100926 (2024).
61. Ouimet, M. et al. *Mycobacterium tuberculosis* induces the miR-33 locus to reprogram autophagy and host lipid metabolism. *Nat. Immunol.* **17**, 677–686 (2016).
62. Wang, W. et al. Ultrastable in-situ silver nanoparticle dressing for effective prevention and treatment of wound infection in emergency. *Eng. Regener.* **5**, 111–123 (2024).

Acknowledgements

The authors gratefully acknowledge the financial support provided by the National Natural Science Foundation of China (22275081, D.Z.; 82372117, Y.W.; 52303381, S.H., 82500159 and 22565018, W.W.), Natural Science Foundation of Guangdong Province of China (2024A1515010464, Y.W.), Natural Science Foundation of Xiamen, China (3502Z202371003, S.H.), and the Fundamental Research Funds for the Central Universities (20720230008, S.H.). The materials used in Figs. 2a–c, 3j, 5a, 7a, and 8a are obtained from Biorender, https://www.biorender.com. Figures 3a and 9 were created by Hangzhou Yanqu Information Technology Co., Ltd. using Cinema 4D (C4D) and Adobe After Effects (AE).

Author contributions

W.W.: Conceptualization, methodology, resources, writing—original draft. W.W., F.L., W.M., Z.L. (Zining Liu), Y.L., Z.L (Zihui Liu), P.W., J.X., and P.C.: Data curation, formal analysis, writing—original draft, writing—review and editing. S.H.: Conceptualization, data curation, formal analysis, review and editing. Y.W.: Conceptualization, data curation, funding acquisition, formal analysis, writing—original draft, writing—review and editing. D.Z.: Conceptualization, data curation, funding acquisition, resources, validation, writing—review and editing.

Competing interests
The authors declare no competing interests.

Additional information
Supplementary information The online version contains supplementary material available at https://doi.org/10.1038/s41467-026-69420-1.

Correspondence and requests for materials should be addressed to Shasha He, Yupeng Wang or Dongfang Zhou.

Peer review information *Nature Communications* thanks Himanshu Shekhar and the other anonymous reviewer for their contribution to the peer review of this work. [A peer review file is available].